arXiv:2507.01762v4 [math.NA] 4 May 2026

GLOBAL ENERGY MINIMIZATION FOR SIMPLEX MESH OPTIMIZATION: A RADIUS RATIO APPROACH TO SLIVER ELIMINATION

A PREPRINT

Dong Wang
School of Mathematics and Computational Science
XiangTan University
China, Xiangtan 411105
wangdongs@smail.xtu.edu.cn

Chunyu Chen
School of Mathematics and Computational Science
XiangTan University
China, Xiangtan 411105
cbtxs@smail.xtu.edu.cn

Huayi Wei*
School of Mathematics and Computational Science, Xiangtan University
National Center of Applied Mathematics in Hunan
Hunan Key Laboratory for Computation and Simulation in Science and Engineering
China, Xiangtan 411105
weihuayi@xtu.edu.cn

ABSTRACT

This paper constructs an energy function for simplex mesh based on the radius ratio and develops a corresponding mesh optimization method. The method combines vertex relocation and connectivity improvement, and can effectively remove slivers and improve the overall mesh quality. Based on the structure of the gradient of the energy function, we design a preconditioner, which reduces the number of iterations and improves the efficiency of the optimization algorithm. Numerical experiments show that the proposed method is effective in both sliver removal and mesh quality improvement.

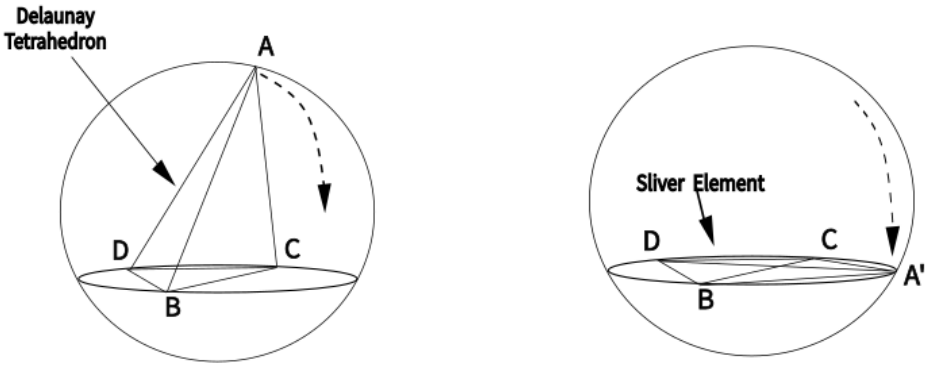
Keywords Sliver · Radius ratio · Energy function · Mesh optimization · Preconditioner

1 Introduction

In numerical computation, mesh plays an important role. Mainstream simulation methods, including the Finite Element Method (FEM) and the Finite Volume Method (FVM), are based on mesh generation [11, 24]. As basic geometric entities, simplices are widely used in many fields, and the study of simplex mesh generation has continued for several decades [29]. Current methods primarily fall into three categories: the Advancing-Front technique [26], spatial decomposition algorithms [32, 36], and Delaunay-based methods [1, 34].

Delaunay algorithms are widely used in mesh generation due to its algorithmic simplicity and broad applicability. However, in three-dimensional cases, it tends to produce ill-shaped tetrahedron that require optimization. Common improvement strategies include Laplacian smoothing, local transformations, and hybrid approaches [18, 25], However, these methods cannot completely remove a type of nearly degenerate element called sliver.The existence of slivers was first pointed out by Cavendish [2]. A sliver has faces that are well-shaped triangles, but its volume is close to zero, and its four vertices are almost coplanar. Despite this, it still satisfies the Delaunay property in a topological sense. Such elements can seriously affect the numerical simulation [33]. To address the sliver problem, many methods have been proposed. For example, Chew [8] introduced a randomized point insertion method, Li [21] proposed a vertex perturbation method, and Cheng [6] developed the sliver exudation method.

In the past two decades, researchers have also studied mesh optimization from the perspective of optimization theory. Examples include variational mesh optimization methods such as Optimal Delaunay Triangulation(ODT) [3, 5]



(a) Delaunay Tetrahedron and its circumsphere (b) Sliver Element is a valid Delaunay Element

Figure 1: Sliver element

and Centroidal Voronoi Tessellation(CVT) [10, 16] algorithms, as well as algebraic quality-based methods such as the Target-Matrix Optimization Paradigm(TMOP) [19, 20]. Although these methods differ in their design ideas, they all define an energy function and formulate mesh optimization as the minimization of an objective function. A high-quality mesh is then obtained by applying numerical optimization methods. However, these approaches are not designed specifically for slivers. As a result, the optimized meshes may still contain slivers. Some researchers have designed energy functions that directly target slivers. For example, Saifeng Ni [6] proposed a shape-matching strategy to construct an energy function. This energy is sensitive to the height of tetrahedral elements and can effectively suppress slivers.

In addition to element height, the radius ratio is also an important quality measure that can effectively identify slivers. In fact, when Cavendish first pointed out the existence of sliver, they introduced a quality metric based on the ratio between the inradius and the circumradius, and used it to determine whether an element is a sliver. This measure can capture the geometric feature that the element volume approaches zero while the edge lengths remain normal. Since then, it has been widely used for the detection and evaluation of slivers, and has become a classical quality metric in this area. In this work, we introduce the radius ratio explicitly into the construction of the energy function, in order to build an optimization model that is highly sensitive to slivers. In addition, based on the structure of the gradient of the energy function, we construct a symmetric positive definite (SPD) and diagonally dominant matrix as a preconditioner, which leads to an efficient global optimization algorithm. The proposed method can be used as a standalone mesh optimization tool, and it can also be applied as a post-processing step for existing optimization methods.

2 Radius Ratio Energy Function

The convex hull of a set of points $\{\boldsymbol{x}_i\}_{i=0}^{d} \subset \mathbb{R}^d$ that do not lie in one hyperplane

$$\tau = \{\boldsymbol{x} = \sum_{i=0}^{d} \lambda_i \boldsymbol{x}_i | 0 \leq \lambda_i \leq 1, \sum_{i=0}^{d} \lambda_i = 1\}$$

is called a geometric d-simplex generated by $\{\boldsymbol{x}_i\}_{i=0}^{d}$. For example, an interval is a 1-simplex, a triangle is a 2-simplex, and a tetrahedron is a 3-simplex.

For a positively-oriented simplex τ in $\mathbb{R}^d$, $d = 2, 3$, the radius ratio metric is defined as follows [2]:

$$\mu = \frac{R}{dr}$$

where R is the circumradius and r is the inradius of τ. $\mu \in [1, +\infty]$ With $\mu = 1$ if and only if τ is equilateral simplex.

Radius ratio metric μ is a function of the coordinates of the simplex vertices. Given a triangulation $\mathcal{T}$ with N_v vertices $\{\boldsymbol{x}_i\}_{i=0}^{N_v-1}$ and N_c simplex $\{\tau_n\}_{n=0}^{N_c-1}$. We can define an energy function of radius ratio metric on the $\mathcal{T}$

$$F = \frac{1}{N_c} \sum_{n=0}^{N_c-1} \mu_n$$

Here we call F is global radius ratio energy function. By minimizing F, we can develop efficient global mesh smoothing algorithm by moving the points in $\mathcal{T}$. The key problem is how to compute the gradient of F about mesh point coordinates. In the following, we derive the gradient of μ_n with respect to each vertex of a d-simplex τ_n, and then obtain the global gradient.

2.1 2D Case

Given a 2D triangulation $\mathcal{T}$ with N_v vertices $\{\boldsymbol{x}_i\}_{i=0}^{N_v-1} \subset \mathbb{R}^2$ and N_c triangles $\{\tau_n\}_{n=0}^{N_c-1}$. For $\forall \tau_n = (\boldsymbol{x}_0, \boldsymbol{x}_1, \boldsymbol{x}_2)$, let $e_0 := (\boldsymbol{x}_1, \boldsymbol{x}_2), e_1 := (\boldsymbol{x}_2, \boldsymbol{x}_0)$ and $e_2 := (\boldsymbol{x}_0, \boldsymbol{x}_1)$ be the three edges of τ_n with length l_0, l_1 and l_2 respectively; $|\tau_n|$ be the area of τ_n.

The circumradius of τ_n is:

$$R_n = \frac{q}{4|\tau_n|}$$

with $q = l_0 l_1 l_2$. The inradius of τ_n is:

$$r_n = \frac{2|\tau_n|}{p}$$

with $p = l_0 + l_1 + l_2$. The radius ratio metric of τ_n is:

$$\mu_n = \frac{R_n}{2r_n} = \frac{pq}{16|\tau_n|^2}$$

Next we compute the gradient μ_n about $\boldsymbol{x}_0$.

$$\nabla_{\boldsymbol{x}_0}\mu_n = \frac{pq}{16|\tau_n|^2}\left(\frac{\nabla_{\boldsymbol{x}_0}p}{p} + \frac{\nabla_{\boldsymbol{x}_0}q}{q} - \frac{2}{|\tau_n|}\nabla_{\boldsymbol{x}_0}|\tau_n|\right)$$

where

$$\begin{aligned}
\nabla_{\boldsymbol{x}_0}p &= \frac{1}{l_1}(\boldsymbol{x}_0 - \boldsymbol{x}_2) + \frac{1}{l_2}(\boldsymbol{x}_0 - \boldsymbol{x}_1) \\
\nabla_{\boldsymbol{x}_0}q &= \frac{q}{l_1^2}(\boldsymbol{x}_0 - \boldsymbol{x}_2) + \frac{q}{l_2^2}(\boldsymbol{x}_0 - \boldsymbol{x}_1) \\
\nabla_{\boldsymbol{x}_0}|\tau_n| &= \frac{1}{2}\boldsymbol{W}(\boldsymbol{x}_2 - \boldsymbol{x}_1)
\end{aligned}$$

with

$$\boldsymbol{W} = \begin{pmatrix} 0 & -1 \\ 1 & 0 \end{pmatrix}$$

We have

$$\nabla_{\boldsymbol{x}_0}\mu_n = \mu_n\left\{\left[\frac{1}{pl_1} + \frac{1}{l_1^2}\right](\boldsymbol{x}_0 - \boldsymbol{x}_2) + \left[\frac{1}{pl_2} + \frac{1}{l_2^2}\right](\boldsymbol{x}_0 - \boldsymbol{x}_1) + \frac{1}{|\tau_n|}\boldsymbol{W}(\boldsymbol{x}_1 - \boldsymbol{x}_2)\right\}$$

For simplicity, we denote

$$\begin{gathered}
c = \frac{1}{|\tau_n|}, c_0 = \frac{1}{pl_0} + \frac{1}{l_0^2}, c_1 = \frac{1}{pl_1} + \frac{1}{l_1^2}, c_2 = \frac{1}{pl_2} + \frac{1}{l_2^2}, \\
c_{01} = c_0 + c_1, c_{02} = c_0 + c_2, c_{12} = c_1 + c_2
\end{gathered}$$

So

$$\nabla_{\boldsymbol{x}_0}\mu_n = \mu_n\left[c_{12}\boldsymbol{x}_0 - (c_2\boldsymbol{I} - c\boldsymbol{W})\boldsymbol{x}_1 - (c_1\boldsymbol{I} + c\boldsymbol{W})\boldsymbol{x}_2\right]$$

Simiarly

$$\begin{aligned}
\nabla_{\boldsymbol{x}_1}\mu_n &= \mu_n\left[c_{20}\boldsymbol{x}_1 - (c_0\boldsymbol{I} - c\boldsymbol{W})\boldsymbol{x}_2 - (c_2\boldsymbol{I} + c\boldsymbol{W})\boldsymbol{x}_0\right] \\
\nabla_{\boldsymbol{x}_2}\mu_n &= \mu_n\left[c_{01}\boldsymbol{x}_2 - (c_1\boldsymbol{I} - c\boldsymbol{W})\boldsymbol{x}_0 - (c_0\boldsymbol{I} + c\boldsymbol{W})\boldsymbol{x}_1\right]
\end{aligned}$$

We denote

$$\boldsymbol{V}_n = [x_0, x_1, x_2, y_0, y_1, y_2]^T$$

Then we can write it in matrix form

$$\nabla_{\boldsymbol{V}_n}\mu_n = \begin{bmatrix} \boldsymbol{A}_n & \boldsymbol{B}_n \\ -\boldsymbol{B}_n & \boldsymbol{A}_n \end{bmatrix}\boldsymbol{V}_n$$

with

$$\boldsymbol{A}_n = \mu_n\begin{pmatrix} c_{12} & -c_2 & -c_1 \\ -c_2 & c_{20} & -c_0 \\ -c_1 & -c_0 & c_{01} \end{pmatrix}, \boldsymbol{B}_n = \mu_n\begin{pmatrix} 0 & -c & c \\ c & 0 & -c \\ -c & c & 0 \end{pmatrix}$$

Matrix $\boldsymbol{A}_n$ is Laplacian and $\boldsymbol{B}_n$ is antisymmetric.

Then, we can assemble the gradient matrix of each element into a global gradient matrix. Therefore, we get the following theorem

Theorem 2.1. *For the energy function*

$$F = \frac{1}{N_c}\sum_{n=0}^{N_c-1}\mu_n$$

of the triangular mesh, we have

$$\nabla_{\boldsymbol{V}} F = \begin{bmatrix} \boldsymbol{A} & \boldsymbol{B} \\ -\boldsymbol{B} & \boldsymbol{A} \end{bmatrix}\begin{bmatrix} \boldsymbol{X} \\ \boldsymbol{Y} \end{bmatrix} = \boldsymbol{G}_F\boldsymbol{V}$$

where $\boldsymbol{A}$ is $N_v \times N_v$ Laplacian matrix, and $\boldsymbol{B}$ is $N_v \times N_v$ antisymmetric matrix,

$$\boldsymbol{V} = [\boldsymbol{X}^T, \boldsymbol{Y}^T]^T, \boldsymbol{X} = [x_0, x_1, \cdots, x_{N_v-1}]^T, \boldsymbol{Y} = [y_0, y_1, \cdots, y_{N_v-1}]^T$$

2.2 3D Case

Given a 3D Tetrahedralization $\mathcal{T}$, consisting of N_v vertices $\{\boldsymbol{x}_i\}_{i=0}^{N_v-1} \subset \mathbb{R}^3$ and N_c tetrahedrons $\{\tau_n\}_{n=0}^{N_c-1}$. For $\forall\tau_n = (\boldsymbol{x}_0, \boldsymbol{x}_1, \boldsymbol{x}_2, \boldsymbol{x}_3)$, let s_0, s_1, s_2, s_3 be the area of triangle opposite to vertices $\boldsymbol{x}_0, \boldsymbol{x}_1, \boldsymbol{x}_2, \boldsymbol{x}_3$; $|\tau_n|$ be the volume of τ_n.

The radius of circumsphere of τ_n is:

$$R_n = \frac{|\boldsymbol{d}_0|}{12|\tau_n|}$$

where

$$\boldsymbol{d}_0 = \boldsymbol{v}_{30}^2\boldsymbol{v}_{10} \times \boldsymbol{v}_{20} + \boldsymbol{v}_{10}^2\boldsymbol{v}_{20} \times \boldsymbol{v}_{30} + \boldsymbol{v}_{20}^2\boldsymbol{v}_{30} \times \boldsymbol{v}_{10}$$

with

$$\boldsymbol{v}_{10} = \boldsymbol{x}_0 - \boldsymbol{x}_1, \boldsymbol{v}_{20} = \boldsymbol{x}_0 - \boldsymbol{x}_2, \boldsymbol{v}_{30} = \boldsymbol{x}_0 - \boldsymbol{x}_3, \boldsymbol{v}^2 = \boldsymbol{v} \cdot \boldsymbol{v}$$

The radius of inside sphere of τ_n is

$$r_n = \frac{3|\tau_n|}{s}$$

with $s = s_0 + s_1 + s_2 + s_3$. The radius ratio metric of τ_n is

$$\mu_n = \frac{R_n}{3r_n} = \frac{s|\boldsymbol{d}_0|}{108|\tau_n|^2}$$

The gradient of μ_n at vertex $\boldsymbol{x}_0$ is

$$\nabla_{\boldsymbol{x}_0}\mu_n = \mu_n\left\{\frac{1}{|\boldsymbol{d}_0|}\nabla_{\boldsymbol{x}_0}|\boldsymbol{d}_0| + \frac{1}{s}\nabla_{\boldsymbol{x}_0}s - \frac{2}{|\tau_n|}\nabla_{\boldsymbol{x}_0}|\tau_n|\right\}$$

where

$$\begin{aligned}\nabla_{\boldsymbol{x}_0}|\boldsymbol{d}_0| =& \frac{1}{|\boldsymbol{d}_0|}\{2[\boldsymbol{d}_0 \cdot (\boldsymbol{v}_{20} \times \boldsymbol{v}_{30})\boldsymbol{v}_{10} + \boldsymbol{d}_0 \cdot (\boldsymbol{v}_{30} \times \boldsymbol{v}_{10})\boldsymbol{v}_{20} + \boldsymbol{d}_0 \cdot (\boldsymbol{v}_{10} \times \boldsymbol{v}_{20})\boldsymbol{v}_{30}] \\ &+ \boldsymbol{d}_0 \times [(\boldsymbol{v}_{30}^2 - \boldsymbol{v}_{20}^2)\boldsymbol{v}_{10} + (\boldsymbol{v}_{10}^2 - \boldsymbol{v}_{30}^2)\boldsymbol{v}_{20} + (\boldsymbol{v}_{20}^2 - \boldsymbol{v}_{10}^2)\boldsymbol{v}_{30}]\}\end{aligned}$$

$$\nabla_{\boldsymbol{x}_0}s = (\frac{\boldsymbol{v}_{31} \cdot \boldsymbol{v}_{30}}{4s_2} + \frac{\boldsymbol{v}_{21} \cdot \boldsymbol{v}_{20}}{4s_3})\boldsymbol{v}_{10} + (\frac{\boldsymbol{v}_{32} \cdot \boldsymbol{v}_{30}}{4s_1} + \frac{\boldsymbol{v}_{12} \cdot \boldsymbol{v}_{10}}{4s_3})\boldsymbol{v}_{20} + (\frac{\boldsymbol{v}_{23} \cdot \boldsymbol{v}_{20}}{4s_1} + \frac{\boldsymbol{v}_{13} \cdot \boldsymbol{v}_{10}}{4s_2})\boldsymbol{v}_{30}$$

$$\nabla_{\boldsymbol{x}_0}|\tau_n| = -\frac{1}{18}\{[\boldsymbol{x}_2 - 2\boldsymbol{x}_3 + \boldsymbol{x}_1]_\times\boldsymbol{v}_{10} + [\boldsymbol{x}_3 - 2\boldsymbol{x}_1 + \boldsymbol{x}_2]_\times\boldsymbol{v}_{20} + [\boldsymbol{x}_1 - 2\boldsymbol{x}_2 + \boldsymbol{x}_3]_\times\boldsymbol{v}_{30}\}$$

We denote

$$\boldsymbol{V}_n = [x_0, x_1, x_2, x_3, y_0, y_1, y_2, y_3, z_0, z_1, z_2, z_3]^T$$

and calculate the matrix form of $\nabla_{\boldsymbol{x}_i}|\boldsymbol{d}_0|, \nabla_{\boldsymbol{x}_i}s, \nabla_{\boldsymbol{x}_i}|\tau_n|$ $(i = 0, 1, 2, 3)$.

For $\nabla_{\boldsymbol{x}_i}|\boldsymbol{d}_0|$, we denote

$$c_{23} = \boldsymbol{d}_0 \cdot (\boldsymbol{v}_{20} \times \boldsymbol{v}_{30}), c_{31} = \boldsymbol{d}_0 \cdot (\boldsymbol{v}_{30} \times \boldsymbol{v}_{10}), c_{12} = \boldsymbol{d}_0 \cdot (\boldsymbol{v}_{10} \times \boldsymbol{v}_{20})$$

$$k_{23} = \boldsymbol{v}_{30}^2 - \boldsymbol{v}_{20}^2, k_{31} = \boldsymbol{v}_{10}^2 - \boldsymbol{v}_{30}^2, k_{12} = \boldsymbol{v}_{20}^2 - \boldsymbol{v}_{10}^2$$

$$[\boldsymbol{d}_0]_\times = \boldsymbol{D}_0 = \begin{bmatrix} 0 & -d_2 & d_1 \\ d_2 & 0 & -d_0 \\ -d_1 & d_0 & 0 \end{bmatrix}$$

so we have

$$\nabla_{\boldsymbol{x}_0}|\boldsymbol{d}_0| = \frac{1}{12|\tau_n|R_n}\{[2(c_{23}+c_{31}+c_{12})+(k_{23}+k_{31}+k_{12})\boldsymbol{D}_0]\boldsymbol{x}_0-(2c_{23}+k_{23}\boldsymbol{D}_0)\boldsymbol{x}_1-(2c_{31}+k_{31}\boldsymbol{D}_0)\boldsymbol{x}_2-(2c_{12}+k_{12}\boldsymbol{D}_0)\boldsymbol{x}_3\}$$

$$\begin{aligned}
\nabla_{\boldsymbol{x}_1}|\boldsymbol{d}_0| &= \frac{1}{12|\tau_n|R_n}\{(-2c_{23}+k_{23}\boldsymbol{D}_0)\boldsymbol{x}_0 + 2c_{23}\boldsymbol{x}_1 - \boldsymbol{v}_{30}^2\boldsymbol{D}_0\boldsymbol{x}_2 + \boldsymbol{v}_{20}^2\boldsymbol{D}_0\boldsymbol{x}_3\} \\
\nabla_{\boldsymbol{x}_2}|\boldsymbol{d}_0| &= \frac{1}{12|\tau_n|R_n}\{(-2c_{31}+k_{31}\boldsymbol{D}_0)\boldsymbol{x}_0 + \boldsymbol{v}_{30}^2\boldsymbol{D}_0\boldsymbol{x}_1 + 2c_{31}\boldsymbol{x}_2 - \boldsymbol{v}_{10}^2\boldsymbol{D}_0\boldsymbol{x}_3\} \\
\nabla_{\boldsymbol{x}_3}|\boldsymbol{d}_0| &= \frac{1}{12|\tau_n|R_n}\{(-2c_{12}+k_{12}\boldsymbol{D}_0)\boldsymbol{x}_0 - \boldsymbol{v}_{20}^2\boldsymbol{D}_0\boldsymbol{x}_1 + \boldsymbol{v}_{10}^2\boldsymbol{D}_0\boldsymbol{x}_2 + 2c_{12}\boldsymbol{x}_3\}
\end{aligned}$$

Then we can write $\nabla_{\boldsymbol{V}_n}|\boldsymbol{d}_0|$ in matrix form

$$\nabla_{\boldsymbol{V}_n}|\boldsymbol{d}_0| = \frac{1}{12|\tau_n|R_n}\begin{bmatrix} \boldsymbol{L} & -d_2\boldsymbol{K} & d_1\boldsymbol{K} \\ d_2\boldsymbol{K} & \boldsymbol{L} & -d_0\boldsymbol{K} \\ -d_1\boldsymbol{K} & d_0\boldsymbol{K} & \boldsymbol{L} \end{bmatrix}\boldsymbol{V}_n$$

with

$$\boldsymbol{L} = \begin{bmatrix} 2c & -2c_{23} & -2c_{31} & -2c_{12} \\ -2c_{23} & 2c_{23} & 0 & 0 \\ -2c_{31} & 0 & 2c_{31} & 0 \\ -2c_{12} & 0 & 0 & 2c_{12} \end{bmatrix}, \boldsymbol{K} = \begin{bmatrix} 0 & -k_{23} & -k_{31} & -k_{12} \\ k_{23} & 0 & -\boldsymbol{v}_{30}^2 & \boldsymbol{v}_{20}^2 \\ k_{31} & \boldsymbol{v}_{30}^2 & 0 & -\boldsymbol{v}_{10}^2 \\ k_{12} & -\boldsymbol{v}_{20}^2 & \boldsymbol{v}_{10}^2 & 0 \end{bmatrix}$$

$c = c_{23} + c_{31} + c_{12}$, matrix $\boldsymbol{L}$ is symmetric, $\boldsymbol{K}$ is antisymmetric.

For $\nabla_{\boldsymbol{x}_i} s$, we denote

$$\begin{aligned}
p_0 &= \frac{\boldsymbol{v}_{31}^2}{4s_2} + \frac{\boldsymbol{v}_{21}^2}{4s_3} + \frac{\boldsymbol{v}_{32}^2}{4s_1}, \quad p_1 = \frac{\boldsymbol{v}_{32}^2}{4s_0} + \frac{\boldsymbol{v}_{02}^2}{4s_3} + \frac{\boldsymbol{v}_{30}^2}{4s_2}, \\
p_2 &= \frac{\boldsymbol{v}_{30}^2}{4s_1} + \frac{\boldsymbol{v}_{10}^2}{4s_3} + \frac{\boldsymbol{v}_{31}^2}{4s_0}, \quad p_3 = \frac{\boldsymbol{v}_{10}^2}{4s_2} + \frac{\boldsymbol{v}_{20}^2}{4s_1} + \frac{\boldsymbol{v}_{21}^2}{4s_0},
\end{aligned}$$

$$\begin{aligned}
q_{01} &= -(\frac{\boldsymbol{v}_{31}\cdot\boldsymbol{v}_{30}}{4s_2} + \frac{\boldsymbol{v}_{21}\cdot\boldsymbol{v}_{20}}{4s_3}), q_{02} = -(\frac{\boldsymbol{v}_{32}\cdot\boldsymbol{v}_{30}}{4s_1} + \frac{\boldsymbol{v}_{12}\cdot\boldsymbol{v}_{10}}{4s_3}), q_{03} = -(\frac{\boldsymbol{v}_{23}\cdot\boldsymbol{v}_{20}}{4s_1} + \frac{\boldsymbol{v}_{13}\cdot\boldsymbol{v}_{10}}{4s_2}), \\
q_{12} &= -(\frac{\boldsymbol{v}_{32}\cdot\boldsymbol{v}_{31}}{4s_0} + \frac{\boldsymbol{v}_{02}\cdot\boldsymbol{v}_{01}}{4s_3}), q_{13} = -(\frac{\boldsymbol{v}_{03}\cdot\boldsymbol{v}_{01}}{4s_2} + \frac{\boldsymbol{v}_{23}\cdot\boldsymbol{v}_{21}}{4s_0}), q_{23} = -(\frac{\boldsymbol{v}_{13}\cdot\boldsymbol{v}_{12}}{4s_0} + \frac{\boldsymbol{v}_{03}\cdot\boldsymbol{v}_{02}}{4s_1})
\end{aligned}$$

We have

$$\begin{aligned}
\nabla_{\boldsymbol{x_0}} s &= p_0\boldsymbol{x}_0 + q_{01}\boldsymbol{x}_1 + q_{02}\boldsymbol{x}_2 + q_{03}\boldsymbol{x}_3, \nabla_{\boldsymbol{x}_1} s = q_{01}\boldsymbol{x}_0 + p_1\boldsymbol{x}_1 + q_{12}\boldsymbol{x}_2 + q_{23}\boldsymbol{x}_3 \\
\nabla_{\boldsymbol{x}_2} s &= q_{02}\boldsymbol{x}_0 + q_{12}\boldsymbol{x}_1 + p_2\boldsymbol{x}_2 + q_{23}\boldsymbol{x}_3, \nabla_{\boldsymbol{x}_3} s = q_{03}\boldsymbol{x}_0 + q_{13}\boldsymbol{x}_1 + q_{23}\boldsymbol{x}_2 + p_3\boldsymbol{x}_3
\end{aligned}$$

Then we can write $\nabla_{\boldsymbol{V}_n} s$ in matrix form

$$\nabla_{\boldsymbol{V}_n}\mu_n = \begin{bmatrix} \boldsymbol{S} & & \\ & \boldsymbol{S} & \\ & & \boldsymbol{S} \end{bmatrix}\boldsymbol{V}_n$$

with

$$\boldsymbol{S} = \begin{bmatrix} p_0 & q_{01} & q_{02} & q_{03} \\ q_{01} & p_1 & q_{12} & q_{13} \\ q_{02} & q_{12} & p_2 & q_{23} \\ q_{03} & q_{13} & q_{23} & p_3 \end{bmatrix}$$

Matrix $\boldsymbol{S}$ is symmetric.

For $\nabla_{\boldsymbol{x}_i}|\tau_n|$, we have

$$\begin{aligned}
\nabla_{\boldsymbol{x}_0}|\tau_n| &= \frac{1}{6}(\boldsymbol{x}_2\times\boldsymbol{x}_1 + \boldsymbol{x}_3\times\boldsymbol{x}_2 + \boldsymbol{x}_1\times\boldsymbol{x}_3), \nabla_{\boldsymbol{x}_1}|\tau_n| = \frac{1}{6}(\boldsymbol{x}_3\times\boldsymbol{x}_0 + \boldsymbol{x}_0\times\boldsymbol{x}_2 + \boldsymbol{x}_2\times\boldsymbol{x}_3), \\
\nabla_{\boldsymbol{x}_2}|\tau_n| &= \frac{1}{6}(\boldsymbol{x}_1\times\boldsymbol{x}_0 + \boldsymbol{x}_3\times\boldsymbol{x}_1 + \boldsymbol{x}_0\times\boldsymbol{x}_3), \nabla_{\boldsymbol{x}_3}|\tau_n| = \frac{1}{6}(\boldsymbol{x}_2\times\boldsymbol{x}_0 + \boldsymbol{x}_0\times\boldsymbol{x}_1 + \boldsymbol{x}_1\times\boldsymbol{x}_2)
\end{aligned}$$

We denote

$$\boldsymbol{C}_0 = \begin{bmatrix} 0 & x_2 & x_3 & x_1 \\ x_3 & 0 & x_0 & x_2 \\ x_1 & x_3 & 0 & x_0 \\ x_2 & x_0 & x_1 & 0 \end{bmatrix}, \boldsymbol{C}_1 = \begin{bmatrix} 0 & y_2 & y_3 & y_1 \\ y_3 & 0 & y_0 & y_2 \\ y_1 & y_3 & 0 & y_0 \\ y_2 & y_0 & y_1 & 0 \end{bmatrix}, \boldsymbol{C}_2 = \begin{bmatrix} 0 & z_2 & z_3 & z_1 \\ z_3 & 0 & z_0 & z_2 \\ z_1 & z_3 & 0 & z_i \\ z_2 & z_0 & z_1 & 0 \end{bmatrix}$$

Then we have

$$\nabla_{\boldsymbol{V}_n}|\tau_n| = \frac{1}{6}\begin{bmatrix} 0 & -\boldsymbol{C}_2 & \boldsymbol{C}_1 \\ \boldsymbol{C}_2 & 0 & -\boldsymbol{C}_0 \\ -\boldsymbol{C}_1 & \boldsymbol{C}_0 & 0 \end{bmatrix}\boldsymbol{V}_n = \boldsymbol{C}\boldsymbol{V}_n$$

Where $|\tau_n|$ is a cubic form with respect to $\boldsymbol{V}_n$, we have the following lemma for cubic forms.

Lemma 2.2. *If the function f is a cubic form with respect to $\boldsymbol{X} = (x_0, x_1, \cdots, x_n)$, then there exist matrix $\boldsymbol{C}$ and $\boldsymbol{E} = \frac{1}{2}(\boldsymbol{C} + \boldsymbol{C}^T)$ such that*

$$\nabla f = \boldsymbol{C}\boldsymbol{X} = \boldsymbol{E}\boldsymbol{X}$$

Proof. If the function f is a cubic form with respect to $\boldsymbol{X} = (x_0, x_1, \cdots, x_n)$, then there exists a third-order matrix $\boldsymbol{U}$ such that

$$f = U_{ijk}x_ix_jx_k$$

Let $W^j_{ik} = \frac{1}{2}(U_{ijk} + U_{kji})$, for any fixed j, $\boldsymbol{W}^j$ is a symmetric matrix, and we have

$$f = W^j_{ik}x_ix_jx_k$$

So we have $\nabla_{x_k} f = U_{ijk}x_ix_j = W^j_{ik}x_ix_j$, let $C_{ki} = U_{ijk}x_j, E_{ki} = W^j_{ik}x_j$, so $\boldsymbol{E} = \frac{1}{2}(\boldsymbol{C} + \boldsymbol{C}^T)$, then we can express ∇f as

$$\nabla f = \boldsymbol{C}\boldsymbol{X} = \boldsymbol{E}\boldsymbol{X}$$

□

From the above theorem, we can get $\nabla_{\boldsymbol{V}_n}|\tau_n| = \frac{1}{2}(\boldsymbol{C} + \boldsymbol{C}^T)\boldsymbol{V}_n$.

$$\frac{1}{2}(\boldsymbol{C} + \boldsymbol{C}^T) = \frac{1}{12}\begin{bmatrix} 0 & \boldsymbol{C}_2^T - \boldsymbol{C}_2 & \boldsymbol{C}_1^T - \boldsymbol{C}_1 \\ \boldsymbol{C}_2 - \boldsymbol{C}_2^T & 0 & \boldsymbol{C}_0^T - \boldsymbol{C}_0 \\ \boldsymbol{C}_1^T - \boldsymbol{C}_1 & \boldsymbol{C}_0^T - \boldsymbol{C}_0 & 0 \end{bmatrix}$$

It is evident that each block matrix in $\frac{1}{2}(\boldsymbol{C} + \boldsymbol{C}^T)$ is an antisymmetric matrix.

From the equation

$$\nabla_{\boldsymbol{x}_0}\mu_n = \mu_n\left\{\frac{1}{|\boldsymbol{d}_0|}\nabla_{\boldsymbol{x}_0}|\boldsymbol{d}_0| + \frac{1}{s}\nabla_{\boldsymbol{x}_0}s - \frac{2}{|\tau_n|}\nabla_{\boldsymbol{x}_0}|\tau_n|\right\}$$

and the gradients $\nabla_{\boldsymbol{V}_n}|\boldsymbol{d}_0|$, $\nabla_{\boldsymbol{V}_n}s$, and $\nabla_{\boldsymbol{V}_n}|\tau_n|$, we can obtain

$$\nabla_{\boldsymbol{V}_n}\mu_n = \mu_n\begin{bmatrix} \boldsymbol{A}_n & \boldsymbol{B}_{0n} & \boldsymbol{B}_{1n} \\ -\boldsymbol{B}_{2n} & \boldsymbol{A}_n & \boldsymbol{B}_{0n} \\ -\boldsymbol{B}_{1n} & -\boldsymbol{B}_{0n} & \boldsymbol{A}_n \end{bmatrix}\boldsymbol{V}_n$$

with

$$\boldsymbol{A}_n = \frac{1}{12|\tau_n|R_n}\boldsymbol{L} + \frac{1}{s}\boldsymbol{S}, \boldsymbol{B}_{0n} = \frac{-d_0}{12|\tau_n|R_n}\boldsymbol{K} - \frac{1}{6|\tau_n|}(\boldsymbol{C}_0^T - \boldsymbol{C}_0),$$

$$\boldsymbol{B}_{1n} = \frac{d_1}{12|\tau_n|R_n}\boldsymbol{K} - \frac{1}{6|\tau_n|}(\boldsymbol{C}_1^T - \boldsymbol{C}_1), \boldsymbol{B}_{2n} = \frac{-d_2}{12|\tau_n|R_n}\boldsymbol{K} - \frac{1}{6|\tau_n|}(\boldsymbol{C}_2^T - \boldsymbol{C}_2)$$

Obviously, $\boldsymbol{A}_n$ is symmetric matrix, and $\boldsymbol{B}_{0n}$, $\boldsymbol{B}_{1n}$, $\boldsymbol{B}_{2n}$ are antisymmetric matrices.

Then, we can assemble the gradient matrix of each element into a global gradient matrix. Therefore, we get the following theorem

Theorem 2.3. *For the energy function*

$$F = \frac{1}{N_c}\sum_{n=0}^{N_c-1}\mu_n$$

of the tetrahedral mesh,we have

$$\nabla_{\boldsymbol{V}} F = \begin{bmatrix} \boldsymbol{A} & \boldsymbol{B}_2 & \boldsymbol{B}_1 \\ -\boldsymbol{B}_2 & \boldsymbol{A} & \boldsymbol{B}_0 \\ -\boldsymbol{B}_1 & -\boldsymbol{B}_0 & \boldsymbol{A} \end{bmatrix} \begin{bmatrix} \boldsymbol{X} \\ \boldsymbol{Y} \\ \boldsymbol{Z} \end{bmatrix} = \boldsymbol{G}_F \boldsymbol{V}$$

where $\boldsymbol{A}$ is $N_v \times N_v$ symmetric matrix, and $\boldsymbol{B}_0$, $\boldsymbol{B}_1$, $\boldsymbol{B}_2$ are $N_v \times N_v$ antisymmetric matrices.

$$\boldsymbol{V} = [\boldsymbol{X}^T, \boldsymbol{Y}^T, \boldsymbol{Z}^T]^T, \boldsymbol{X} = [x_0, x_1, \cdots, x_{N_v-1}]^T, \boldsymbol{Y} = [y_0, y_1, \cdots, y_{N_v-1}]^T, \boldsymbol{Z} = [z_0, z_1, \cdots, z_{N_v-1}]^T$$

.

2.3 Anisotropic case

The radius ratio energy function can be extended to anisotropic mesh. For a triangle element $\tau_n = (\boldsymbol{x}_0, \boldsymbol{x}_1, \boldsymbol{x}_2)$ in a two-dimensional triangulation $\mathcal{T}$, the radius ratio is

$$\mu_n = \frac{R_n}{2r_n} = \frac{pq}{16|\tau_n|^2}$$

Let $\boldsymbol{M}(\boldsymbol{x})$ be the anisotropic metric at point $\boldsymbol{x}$. To use a consistent metric within each element, we define the element metric as the average of the vertex metrics:

$$\boldsymbol{M} = \frac{\boldsymbol{M}(\boldsymbol{x}_0) + \boldsymbol{M}(\boldsymbol{x}_1) + \boldsymbol{M}(\boldsymbol{x}_2)}{3} = \begin{bmatrix} m_0 & m_2 \\ m_2 & m_1 \end{bmatrix}$$

Under this metric, the lengths of the three edges of the triangle can be written as

$$l_0 = \sqrt{< \boldsymbol{u}_1 - \boldsymbol{u}_2, \boldsymbol{M}(\boldsymbol{u}_1 - \boldsymbol{u}_2) >}, l_1 = \sqrt{< \boldsymbol{u}_0 - \boldsymbol{u}_2, \boldsymbol{M}(\boldsymbol{u}_0 - \boldsymbol{u}_2) >}, l_2 = \sqrt{< \boldsymbol{u}_0 - \boldsymbol{u}_1, \boldsymbol{M}(\boldsymbol{u}_0 - \boldsymbol{u}_1) >}$$

The area of the element under the anisotropic metric satisfies

$$|\tau_n| = \sqrt{\det \boldsymbol{M}} |\tau_n|_\Omega$$

where $|\tau_n|_\Omega$ is the area under the Euclidean metric.

Based on these definitions, the gradients of the quantities in the radius ratio with respect to the vertex positions can be derived. The derivation is similar to the two-dimensional isotropic case. Finally, we obtain

$$\nabla_{\boldsymbol{V}_n} \mu_n = \begin{bmatrix} m_0 \boldsymbol{A}_n & m_2 \boldsymbol{A}_n + \boldsymbol{B}_n \\ m_2 \boldsymbol{A}_n + \boldsymbol{B}_n^T & m_1 \boldsymbol{A}_n \end{bmatrix} \boldsymbol{V}_n$$

with

$$\boldsymbol{A}_n = \mu_n \begin{pmatrix} c_{12} & -c_2 & -c_1 \\ -c_2 & c_{20} & -c_0 \\ -c_1 & -c_0 & c_{01} \end{pmatrix}, \boldsymbol{B}_n = \mu_n \begin{pmatrix} 0 & -c & c \\ c & 0 & -c \\ -c & c & 0 \end{pmatrix}$$

$$\boldsymbol{V}_n = [x_0, x_1, x_2, y_0, y_1, y_2]^T$$

$$c = \frac{\sqrt{\det \boldsymbol{M}}}{|\tau_n|}, c_0 = \frac{1}{pl_0} + \frac{1}{l_0^2}, c_1 = \frac{1}{pl_1} + \frac{1}{l_1^2}, c_2 = \frac{1}{pl_2} + \frac{1}{l_2^2}$$

$$c_{01} = c_0 + c_1, c_{02} = c_0 + c_2, c_{12} = c_1 + c_2$$

For a tetrahedral element $\tau_n = (\boldsymbol{x}_0, \boldsymbol{x}_1, \boldsymbol{x}_2, \boldsymbol{x}_3)$ in a three-dimensional tetrahedralization $\mathcal{T}$, the radius ratio is

$$\mu_n = \frac{R_n}{3r_n} = \frac{s|\boldsymbol{d}_0|}{108|\tau|^2}$$

We define the anisotropic metric of the element as the average of the vertex metrics:

$$\boldsymbol{M} = \frac{\boldsymbol{M}(\boldsymbol{x}_0) + \boldsymbol{M}(\boldsymbol{x}_1) + \boldsymbol{M}(\boldsymbol{u}_2) + \boldsymbol{M}(\boldsymbol{x}_3)}{4} = \begin{bmatrix} m_{00} & m_{01} & m_{02} \\ m_{01} & m_{11} & m_{12} \\ m_{02} & m_{12} & m_{22} \end{bmatrix}$$

Based on this metric, the gradient of the radius ratio of the anisotropic tetrahedral element with respect to the vertex positions can be derived. It can be written in a matrixvector form. Let

$$\boldsymbol{V}_n = [x_0, x_1, x_2, x_3, y_0, y_1, y_2, y_3, z_0, z_1, z_2, z_3]^T$$

then the element gradient can be expressed as

$$\nabla_{\boldsymbol{V}_n}\mu_n = \mu_n \begin{bmatrix} \boldsymbol{A}_0 & \boldsymbol{B}_2 & \boldsymbol{B}_1 \\ \boldsymbol{B}_2^T & \boldsymbol{A}_1 & \boldsymbol{B}_0 \\ \boldsymbol{B}_1^T & \boldsymbol{B}_0^T & \boldsymbol{A}_2 \end{bmatrix} \boldsymbol{V}_n$$

where $\boldsymbol{A}_i, \boldsymbol{B}_i$ $(i = 0, 1, 2)$ are both symmetric matrices. Since the derivation is similar to the isotropic case, it is omitted here.

Under an anisotropic metric, both two-dimensional triangular elements and three-dimensional tetrahedral elements admit a radius ratio μ and its gradient with respect to the vertex coordinates.Consider a simplex mesh $\mathcal{T}$ with N_v vertices $\{\boldsymbol{x}_i\}_{i=0}^{N_v-1} \subset \mathbb{R}^3$ and N_c elements $\{\tau_n\}_{n=0}^{N_c-1}$. We define the global anisotropic radius ratio energy as

$$F = \frac{1}{N_c}\sum_{n=0}^{N_c-1}\mu_n$$

This energy sums the anisotropic radius ratios of all elements and reflects the overall shape quality of the mesh under the given anisotropic metric.

Similar to the isotropic case, the gradient of the radius ratio for each element can be written in a matrixvector form. Therefore, the gradient of the global anisotropic energy can be obtained by assembling the element gradient matrices into a global matrix, in the same way as in Theorem 2.1 and Theorem 2.3, and then computing the gradient of the energy function.

3 Preconditioner design

In this work, one key step in mesh optimization is to compute the minimizer of the energy function and obtain updated vertex positions. Since the gradient of the energy function can be computed, we can apply first-order numerical optimization methods, such as gradient descent, quasi-Newton methods, and nonlinear conjugate gradient (NLCG) methods. From the derivation in Section 2, the gradient of the energy can be written in a matrix-vector form. The matrix contains partial Hessian information. Based on this structure, we design a preconditioning operator. This idea is mainly inspired by fast algorithms developed for Optimal Delaunay Triangulation (ODT) [4]and Centroidal Voronoi Tessellation (CVT) [16].

From Theorem 2.1, the gradient of the radius ratio energy for a two-dimensional simplex mesh can be written as

$$\nabla_{\boldsymbol{V}}F = \begin{bmatrix} \boldsymbol{A} & \boldsymbol{B} \\ -\boldsymbol{B} & \boldsymbol{A} \end{bmatrix} \begin{bmatrix} \boldsymbol{X} \\ \boldsymbol{Y} \end{bmatrix} = \boldsymbol{G}_F\boldsymbol{V}$$

Based on this, the Hessian matrix can be written in the form

$$\boldsymbol{H} = \nabla_{\boldsymbol{V}}^2 F = \boldsymbol{G}_F + \frac{\partial \boldsymbol{G}_F}{\partial \boldsymbol{V}}\boldsymbol{V}$$

The term $\frac{\partial \boldsymbol{G}_F}{\partial \boldsymbol{V}}\boldsymbol{V}$ describes how $\boldsymbol{G}_F$ changes with the vertex coordinates $\boldsymbol{V}$. This term is difficult to compute. In practice, we treat $\boldsymbol{G}_F$ as a constant matrix at the current iteration. Then $\boldsymbol{G}_F$ is used as the main approximation of the Hessian.

In $\boldsymbol{G}_F$, the matrix $\boldsymbol{B}$ is antisymmetric and does not contribute to the quadratic form. The quadratic form is fully determined by $\boldsymbol{A}$. Therefore, when constructing the preconditioner, we can ignore $\boldsymbol{B}$ and keep only the symmetric dominant part. The preconditioner is chosen as

$$\boldsymbol{P} = \begin{bmatrix} \boldsymbol{A} & \\ & \boldsymbol{A} \end{bmatrix}$$

From Theorem 2.3, the gradient of the radius ratio energy for a three-dimensional simplex mesh can be written as

$$\nabla_{\boldsymbol{V}}F = \begin{bmatrix} \boldsymbol{A} & \boldsymbol{B}_2 & \boldsymbol{B}_1 \\ -\boldsymbol{B}_2 & \boldsymbol{A} & \boldsymbol{B}_0 \\ -\boldsymbol{B}_1 & -\boldsymbol{B}_0 & \boldsymbol{A} \end{bmatrix} \begin{bmatrix} \boldsymbol{X} \\ \boldsymbol{Y} \\ \boldsymbol{Z} \end{bmatrix} = \boldsymbol{G}_F\boldsymbol{V}$$

In the two-dimensional case, diagonal blocks can be directly used as the preconditioner. In three dimensions, the block matrix $\boldsymbol{A}$ has a more complex structure. It is assembled from the element-wise matrices $\boldsymbol{A}_n$, where

$$\boldsymbol{A}_n = \frac{1}{12|\tau_n|R_n}\boldsymbol{L} + \frac{1}{s}\boldsymbol{S}$$

$\boldsymbol{S}$ is Laplacian matrix, and the entries of $\boldsymbol{L}$ are given by

$$c_{ij} = \boldsymbol{d}_0 \cdot (\boldsymbol{v}_{i0} \times \boldsymbol{v}_{j0})$$

which are related to face normals. When the element quality is poor, c_{ij} may become negative.This makes $\boldsymbol{L}$ indefinite and affects the stability of $\boldsymbol{A}_n$.

To address this issue, we modify $\boldsymbol{L}$ by taking absolute values:

$$\boldsymbol{L}_{\text{abs}} = \begin{bmatrix} 2(|c_{23}| + |c_{31}| + c_{12}|) & -2|c_{23}| & -2|c_{31}| & -2|c_{12}| \\ -2|c_{23}| & 2|c_{23}| & 0 & 0 \\ -2|c_{31}| & 0 & 2|c_{31}| & 0 \\ -2|c_{12}| & 0 & 0 & 2|c_{12}| \end{bmatrix}$$

and define

$$\boldsymbol{A}_{n,\text{abs}} = \frac{1}{12|\tau_n|R_n}\boldsymbol{L}_{\text{abs}} + \frac{1}{s}\boldsymbol{S}$$

After assembling $\boldsymbol{A}_{n,abs}$ over all elements, we obtain a global matrix $\boldsymbol{A}_{\text{abs}}$, which is Laplacian. Based on this, we choose the following block diagonal form as the preconditioner:

$$\boldsymbol{P} = \begin{bmatrix} \boldsymbol{A}_{abs} & & \\ & \boldsymbol{A}_{abs} & \\ & & \boldsymbol{A}_{abs} \end{bmatrix}$$

In both two and three dimensions, the preconditioner $\boldsymbol{P}$ is a sparse and symmetric positive semi-definite Laplacian matrix. To make it symmetric positive definite in practice, we can fix the boundary nodes. If the boundary nodes are not fixed, we can apply a projection operator to restrict their motion to the geometric constraint manifold.

For each mesh node, we define a local 3×3 projection matrix $\boldsymbol{T}_i$:

$$\begin{cases} \boldsymbol{T}_i = \boldsymbol{I}_3 & \text{if } \boldsymbol{x}_i \text{ is an interior node} \\ \boldsymbol{T}_i = \boldsymbol{I}_3 - \boldsymbol{n}_i\boldsymbol{n}_i^T & \text{if } \boldsymbol{x}_i \text{ is on a surface boundary} \\ \boldsymbol{T}_i = \boldsymbol{t}_i\boldsymbol{t}_i^T & \text{if } \boldsymbol{x}_i \text{ is on a curve boundary} \end{cases}$$

where $\boldsymbol{n}_i$ is the unit normal vector at a surface boundary node, and $\boldsymbol{t}_i$ is the unit tangent vector at a curve boundary node. These matrices can be assembled into a global projection matrix $\boldsymbol{\Pi}$.

By either fixing boundary nodes or applying the projection matrix $\boldsymbol{\Pi}$, the preconditioner becomes symmetric positive definite. The resulting linear system can then be solved efficiently by the conjugate gradient method [27] or algebraic multigrid methodcite [23, 31], which makes the approach suitable for large-scale mesh optimization problems.

4 Energy Optimization

We call our mesh optimization algorithm the Radius Ratio Energy (RRE) mesh optimization algorithm. The RRE mesh optimization algorithm consists of two main parts:

1. Mesh vertex relocation based on the radius ratio energy
2. Connectivity update

In the vertex relocation step, we define an energy function based on the radius ratio of mesh elements and compute its gradient with respect to the vertex coordinates. Then, we apply a first-order optimization method to minimize the energy. This gives new vertex positions and updates the mesh.

The BFGS method is one of the most widely used quasi-Newton methods. In this work, we mainly use its preconditioned limited-memory version (PLBFGS). Below we present one iteration of the PLBFGS method. More details can be found in [22, 28].

Here, $\boldsymbol{P}_k$ is the chosen preconditioner, and

$$\boldsymbol{H}_k = \frac{\boldsymbol{s}_{k-1}^T\boldsymbol{y}_{k-1}}{\boldsymbol{y}_{k-1}^T\boldsymbol{y}_{k-1}}$$

The step size α_k is obtained by a line search that satisfies the strong Wolfe conditions, with initial guess $\alpha_k = 1$.

In addition to the PLBFGS method, we also use the preconditioned nonlinear conjugate gradient (PNLCG) method [15, 28]. We first describe one iteration from step $k-1$ to step k ($k = 1, 2, \cdots$) without a preconditioner.

Algorithm 1 PLBFGS Algorithm

1: At current point $\boldsymbol{x}_k$, compute the gradient $\boldsymbol{g}_k$
2: Set

$$\delta = \begin{cases} 0, & \text{if } k \leq m \\ k-m, & \text{if } k > m \end{cases} ; L = \begin{cases} k, & \text{if } k \leq m \\ m, & \text{if } k > m \end{cases} ; \boldsymbol{q} = \boldsymbol{g}_k$$

3: Backward loop:
4: **for** $i = L-1, L-2, \cdots, 1, 0$: **do**
5: $\quad j = i + \delta$
6: $\quad \alpha_i = \rho_j \boldsymbol{s}_j^T \boldsymbol{q}$
7: $\quad \boldsymbol{q}_i = \boldsymbol{q} - \alpha_i \boldsymbol{y}_j$
8: **end for**
9: If no preconditioner is used, set $\boldsymbol{r} = \boldsymbol{H}_k \boldsymbol{q}$, if a preconditioner is used, solve $\boldsymbol{P}_k \boldsymbol{r} = \boldsymbol{q}$
10: Forward Loop:
11: **for** $i = 0, 1, 2, \cdots, L-2, L-1$: **do**
12: $\quad j = i + \delta$
13: $\quad \beta_j = \rho_j \boldsymbol{y}_j^T \boldsymbol{r}$
14: $\quad \boldsymbol{r} = \boldsymbol{r} + (\alpha_i - \beta_i)\boldsymbol{s}_j$
15: **end for**
16: Set the search direction $\boldsymbol{d}_k = -\boldsymbol{r}$. Use a line search to find the step size α_k, and update $\boldsymbol{x}_{k+1} = \boldsymbol{x}_k + \alpha_k \boldsymbol{d}_k$
17: Compute $\boldsymbol{s}_k = \boldsymbol{x}_{k+1} - \boldsymbol{x}_k$,$\boldsymbol{y}_k = \boldsymbol{g}_{k+1} - \boldsymbol{g}_k$ and store the most recent m pairs of vectors.

Algorithm 2 NLCG Algorithm

1: At the current point $\boldsymbol{x}_k$, compute the gradient $\boldsymbol{g}_k$
2: Compute the scalar coefficient β_k, and update the search direction $\boldsymbol{d}_k = -\boldsymbol{g}_k + \beta_k \boldsymbol{d}_{k-1}$
3: Use a line search to compute the step size α_k, and update $\boldsymbol{x}_k = \boldsymbol{x}_{k-1} + \alpha_k \boldsymbol{d}_k$

Here, α_k is obtained by a line search that satisfies the strong Wolfe conditions, with initial guess $\alpha_k = 1$. The choice of β_k has a strong effect on performance [15]. Common choices include the PolakRibière(β_k^{PR}) [30], HestenesStiefel(β_k^{HS}) [17], FletcherReeves(β_k^{FR}) [13], and Dai-Yuan(β_k^{DY}) [9] formulas. In this work, we use the PolakRibière formula:

$$\beta_k^{PR} = \frac{\boldsymbol{g}_k^T (\boldsymbol{g}_k - \boldsymbol{g}_{k-1})}{\boldsymbol{g}_{k-1}^T \boldsymbol{g}_{k-1}}$$

Next, we give the iteration with a preconditioner. Let the preconditioned gradient $\boldsymbol{z}_k$ be defined by solving $\boldsymbol{P}_k \boldsymbol{z}_k = \boldsymbol{g}_k$ and set the initial search direction $\boldsymbol{d}_0 = -\boldsymbol{z}_0$. Then one iteration from step $k-1$ to step k is:

Algorithm 3 PNLCG Algorithm

1: At the current point $\boldsymbol{x}_k$, compute the preconditioned gradient $\boldsymbol{z}_k$.
2: Compute the scalar coefficient β_k, and update the search direction $\boldsymbol{d}_k = -\boldsymbol{z}_k + \beta_k \boldsymbol{d}_{k-1}$
3: Use a line search to compute α_k, and update $\boldsymbol{x}_{k+1} = \boldsymbol{x}_k + \alpha_k \boldsymbol{d}_k$

When a preconditioner is used, β_k is also based on the preconditioned gradient. The PR-type formula used in this work is

$$\beta_k^{PR} = \frac{\boldsymbol{z}_k^T (\boldsymbol{g}_k - \boldsymbol{g}_{k-1})}{\boldsymbol{z}_{k-1}^T \boldsymbol{g}_{k-1}}$$

The main stopping criterion for vertex relocation is $\|F_{k+1} - F_k\| < \varepsilon$, where ε is usually set to 10^{-6}. After convergence of the vertex relocation step, we update the mesh connectivity. Given an initial connectivity, we improve it by flip operations. These operations are applied to tetrahedral mesh, including 2-3 flips and 3-2 flips [7]. A flip is accepted if it reduces the average element energy. We examine all edges and faces that satisfy the flip conditions, and repeat until no further energy reduction is possible.

After updating the connectivity, we perform vertex relocation again. These two steps are applied in an alternating way. The process stops when no flip operation can further reduce the energy after the relocation step.

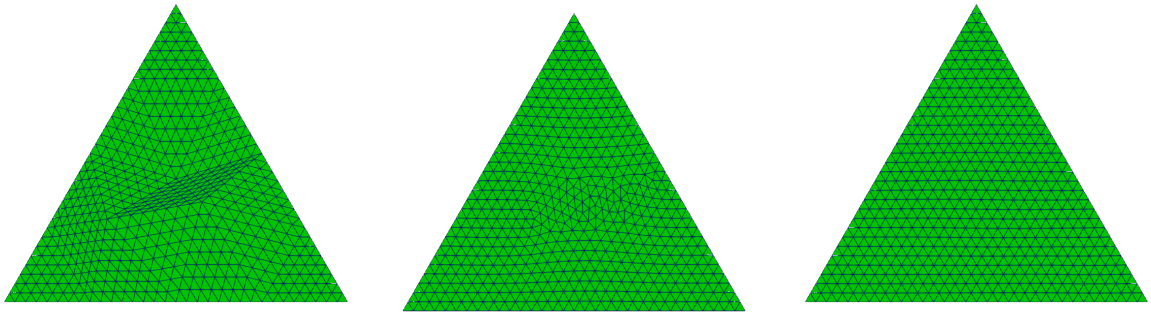
5 Experiments

We implement the proposed algorithm in Python based on the open-source CAX core library FEALPy [35]. All experiments are carried out on a laptop running Ubuntu 22.04, with an AMD Ryzen 7 7735H CPU (3.2 GHz, 16 MB cache) and 16 GB DDR5 RAM (5600 MHz).

Section 5.1 presents examples of two-dimensional triangular mesh, Section 5.2 presents examples of three-dimensional tetrahedral mesh, and Section 5.3 presents examples of anisotropic mesh. In the following, mesh quality refers to the distribution of the element radius ratio. During optimization, the energy function is constructed using the radius ratio $\mu = \frac{R}{dr}$. For convenience in statistics and visualization, we report results using $\frac{dr}{R} \in (0, 1]$. Unless otherwise stated, we use the L-BFGS method and its preconditioned version to solve the energy minimization problem in all examples.

5.1 2D TriangleMesh

Two-dimensional Delaunay triangulations do not produce slivers. Our main focus is on tetrahedral mesh. Therefore, for triangular mesh, we only perform vertex relocation and use these examples to show the effectiveness of the method in improving mesh quality.

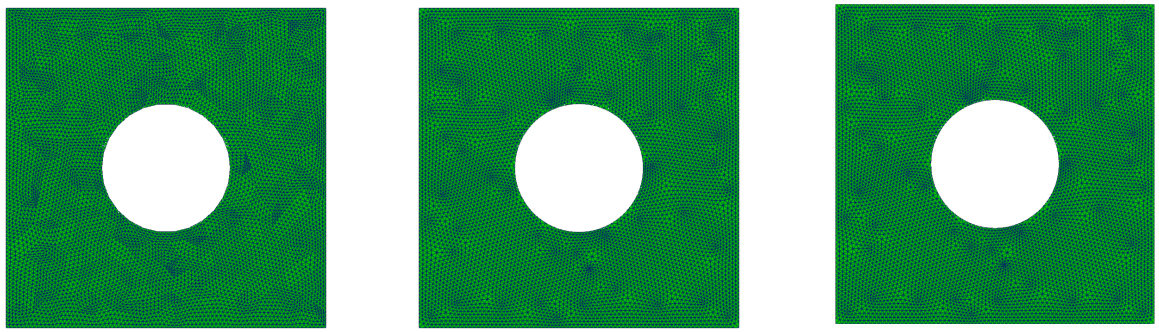


(a) initial mesh (b) ODT local mesh smoothing (c) RRE optimization

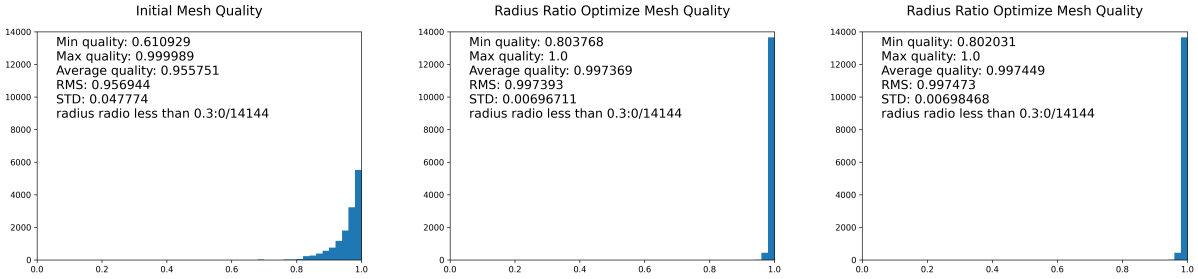
Figure 2: Comparison of mesh obtained by local and global methods

Following the setup in Chen and Holst [4], we move three interior nodes to perturb a uniform mesh of equilateral triangles, and then apply global refinement to obtain Fig. 2 (a). We then optimize the mesh using a local ODT method and the radius ratio method. Fig. 2 (b) shows the result of the local ODT method (a simple Python implementation). This method relies only on local mesh information and performs smoothing by minimizing a local energy associated with each vertex or element. Although each iteration guarantees a decrease of the local energy, this decrease is restricted to a small neighborhood and does not necessarily lead to a reduction of the global energy over the entire mesh. As a result, the optimization process may converge to a configuration that is locally optimal but not globally optimal. Once such a locally stable state is reached, the algorithm may terminate even though further global improvement is still possible. As observed in Fig. 2 (b), the overall mesh quality is improved compared with the initial mesh, but some triangles still deviate from the equilateral shape. Fig. 2 (c) shows the result of the radius ratio method. This method defines a global energy based on the radius ratio and minimizes it using the L-BFGS method. All free nodes are updated together, so global energy decreases over the whole mesh. For this example, the mesh topology is already optimal, so the method converges to a mesh of equilateral triangles. This example shows that, compared with methods based only on local information, a global energy method has a stronger ability to improve the mesh and can achieve higher quality.

Fig. 3 shows a square domain with a circular hole. The initial mesh is generated by Gmsh [14]. To test the ability of the method to improve poor elements, we add random perturbations and apply global refinement. As a result, the initial mesh contains a certain number of low-quality elements. The results in Fig. 3 (b) and (e) show that the number of low-quality elements is greatly reduced, and the minimum radius ratio is clearly improved. The optimized mesh is also more uniform, and the element shapes are closer to regular ones. Fig. 3 (c) and (f) show the results with the preconditioner. The results are almost the same as those without the preconditioner.



(a) initial mesh (b) RRE (c) Precondition RRE



(d) Quality of initial mesh (e) Quality of RRE (f) Quality of Precondition RRE

Figure 3: Square domain with a circular hole

Table 1: Optimization results of two-dimensional examples

Model	Method	Min radius ratio	Mean radius ratio	Iteration count	Times(sec.)
Triangle Domain	Init	0.490	0.896	/	/
	RRE	1.0	1.0	52	0.039
	Precondition RRE	1.0	1.0	10	0.046
Square domain with a circular hole	Init	0.611	0.956	/	/
	RRE	0.804	0.997	193	1.436
	Precondition RRE	0.802	0.997	72	2.119

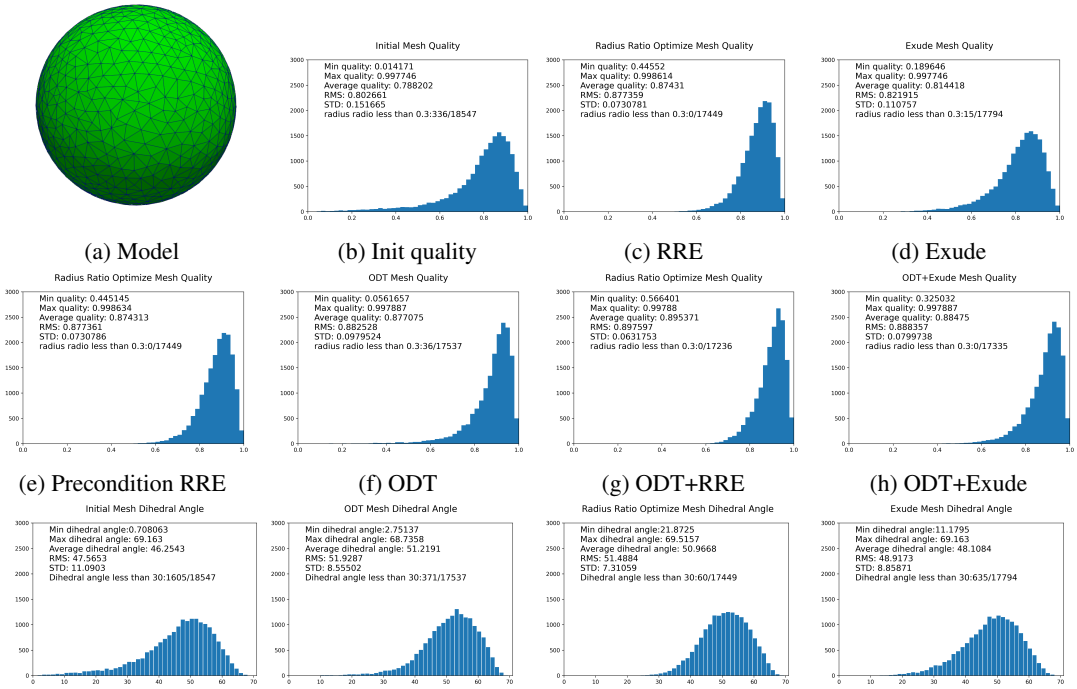
Table 1 lists the results for the two-dimensional examples. In terms of iteration counts, the use of the preconditioner reduces the number of iterations. Here, the iteration count is not the number of L-BFGS iterations. Instead, it is the number of calls to the radius ratio energy function during the Wolfe line search. In one L-BFGS iteration, the line search may call the energy function several times. Therefore, this count better reflects the efficiency of the algorithm. However, since the problem size is small, the cost of building the preconditioner is relatively high, and there is no clear advantage in total computation time. In the tetrahedral mesh examples, we will present more tests to show the benefit of the preconditioner in improving efficiency.

5.2 3D TetrahedronMesh

For tetrahedral mesh optimization, the workflow follows Chapter 4 and consists of two steps: vertex relocation and connectivity update.

Fig. 4, 5, 6 show three examples: a unit sphere, an L-shaped domain, and the intersection of 12 spheres. The initial mesh are generated by CGAL [12]. In addition to the RRE method, we compare with the ODT method and the Sliver Exude method provided by CGAL. The Exude method is designed to remove slivers. These comparisons allow a more complete evaluation of the RRE method in improving element quality and removing slivers.

Subfigures (c), (d), and (f) show the distributions of the radius ratio after RRE, Exude, and ODT, respectively. The results show that:

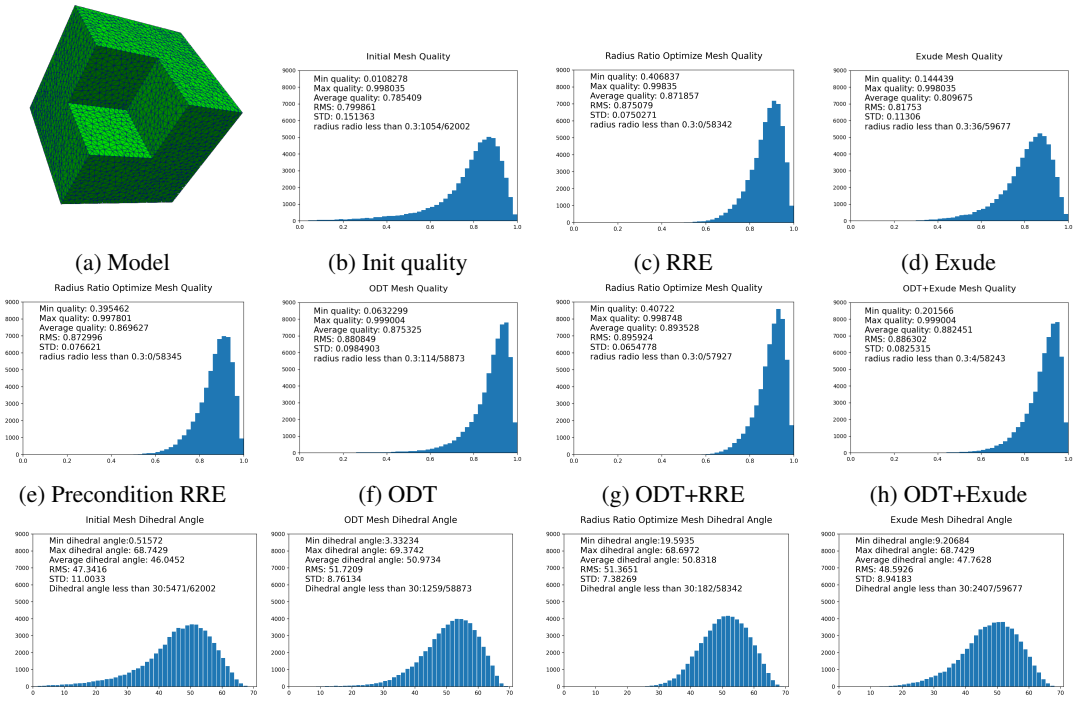


(a) Model (b) Init quality (c) RRE (d) Exude

(e) Precondition RRE (f) ODT (g) ODT+RRE (h) ODT+Exude

(i) Init min dihedral angle (j) ODT min dihedral angle (k) RRE min dihedral angle (l) Exude min dihedral angle

Figure 4: Sphere

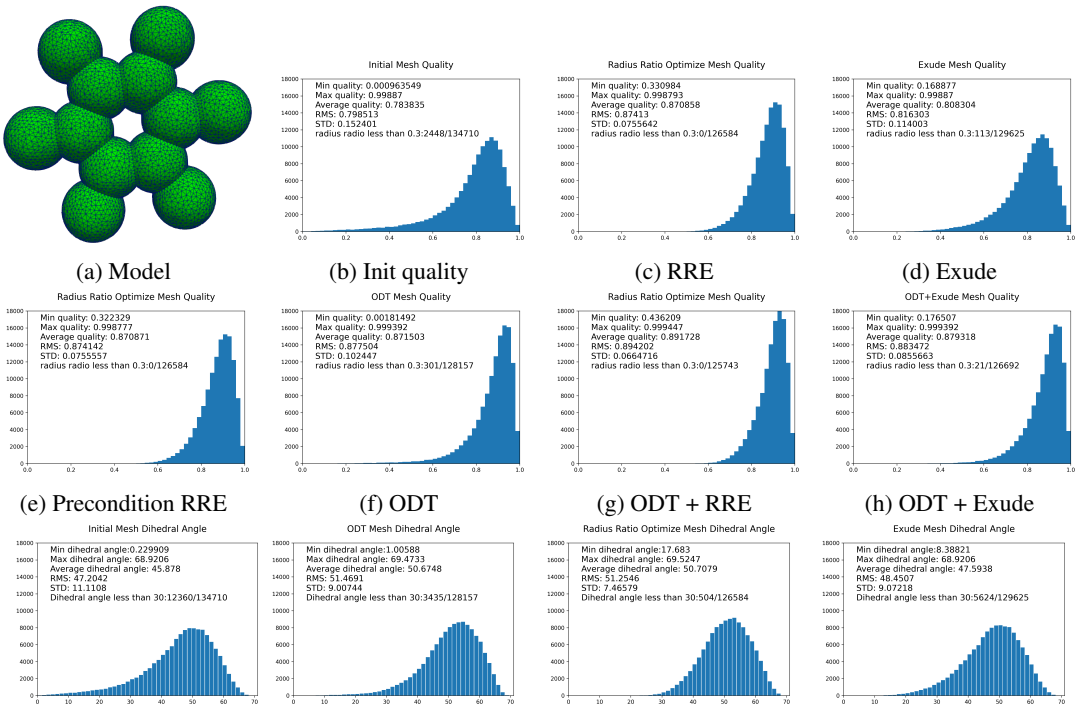


(a) Model (b) Init quality (c) RRE (d) Exude

(e) Precondition RRE (f) ODT (g) ODT+RRE (h) ODT+Exude

(i) Init min dihedral angle (j) ODT min dihedral angle (k) RRE min dihedral angle (l) Exude min dihedral angle

Figure 5: L-shape



(a) Model (b) Init quality (c) RRE (d) Exude

(e) Precondition RRE (f) ODT (g) ODT + RRE (h) ODT + Exude

(i) Init min dihedral angle (j) ODT min dihedral angle (k) RRE min dihedral angle (l) Exude min dihedral angle

Figure 6: intersection of 12 spheres

- ODT improves the overall mesh quality and shifts the distribution toward higher values, but its effect on slivers is limited. A long low-quality tail still remains.
- Exude focuses on removing slivers. It improves the worst elements, but has limited effect on the overall distribution.
- RRE improves both the overall quality and the removal of slivers. It increases the average quality and reduces slivers at the same time.

Subfigures (g) and (h) show the results of combining RRE and Exude with ODT. ODT+Exude improves the worst elements, but the overall distribution does not change much. In contrast, RRE applied after ODT can further remove remaining slivers and continue to improve global distribution.

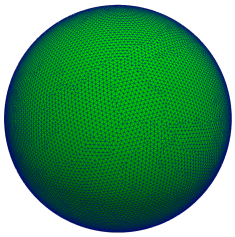
In addition to the radius ratio, we also use the minimum dihedral angle as a secondary quality measure. From subfigures (i), (j), (k), and (l), we see that ODT gives limited improvement in the minimum dihedral angle, while Exude and RRE both improve it clearly. The improvement by RRE is more significant.

Table 2 gives a further comparison in terms of quality improvement and efficiency. In all three examples, RRE gives higher minimum radius ratio and minimum dihedral angle than the other methods. In terms of efficiency, the running time of RRE is close to that of ODT. The Exude method is faster, but it focuses only on sliver removal. RRE improves both global quality and sliver removal, and its effect is close to the combined ODT+Exude method, with good overall efficiency.

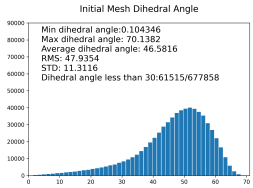
Table 2 also compares the results with and without the preconditioner. As in the two-dimensional case, the iteration count refers to the number of calls to the energy function during the Wolfe line search. This measure better reflects the computational cost. With preconditioner, the number of iterations is clearly reduced, and the running time is also shorter. This shows that the preconditioner improves convergence. The reduction in time is smaller than the reduction in iteration count, because the problem size is small and the cost of building the preconditioner is relatively high. It can also be seen that the final results are similar with and without preconditioner. This means that the preconditioner does not change the solution itself. Its role is to improve the search direction and accelerate convergence. Overall, the preconditioner improves efficiency while keeping the same optimization result.

Table 2: Optimization Result Statistics

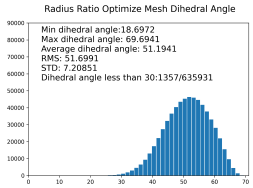
Model	Method	RRE Iteration count/ Flip count	Num of cell	Min dihedral angle(deg.)	Min radius ratio	Time(sec.)
Sphere	Init	/	18547	0.708	0.014	/
	ODT	/	17537	2.751	0.056	16.96
	Exude	/	17794	11.18	0.190	8.63
	RRE	112/2	17449	21.87	0.446	7.88
	Precondition RRE	50/2	17449	21.87	0.445	4.64
	ODT+RRE	68/1	17236	27.76	0.566	21.43
	ODT+Exude	/	17335	15.13	0.325	23.35
Lshape	Init	/	62002	0.516	0.011	/
	ODT	/	58873	3.332	0.063	59.56
	Exude	/	59677	9.207	0.202	31.20
	RRE	222/3	58342	19.59	0.407	50.98
	Precondition RRE	131/3	58345	18.87	0.395	33.66
	ODT+RRE	93/2	57927	18.76	0.407	81.34
	ODT+Exude	/	58243	9.25	0.202	81.80
Intersection of 12 spheres	Init	/	134710	0.230	9.63e-4	/
	ODT	/	128157	1.006	0.002	123.71
	Exude	/	129625	8.388	0.169	69.24
	RRE	225/3	126584	17.68	0.331	116.43
	Precondition RRE	131/3	126584	16.95	0.322	100.10
	ODT+RRE	118/2	125743	20.27	0.436	183.17
	ODT+Exude	/	126692	7.57	0.177	174.94



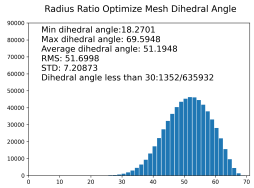
(a) Model



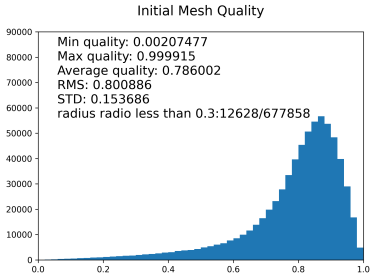
(b) Init min dihedral angle



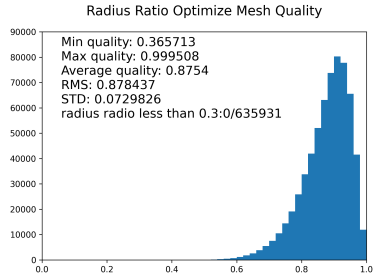
(c) RRE min dihedral angle



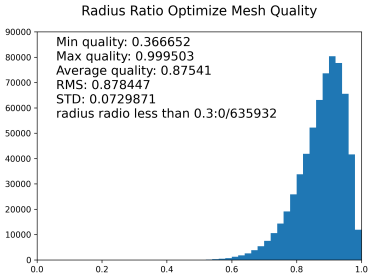
(d) Precondition RRE min dihedral angle



(e) Init quality

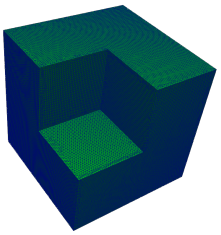


(f) RRE

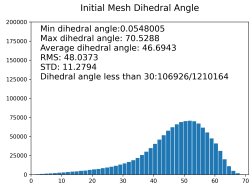


(g) Precondition RRE

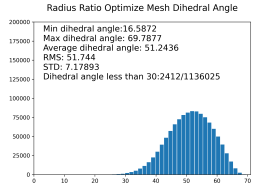
Figure 7: Sphere large scale mesh



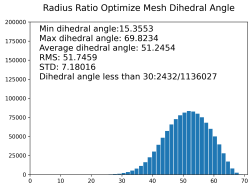
(a) Model



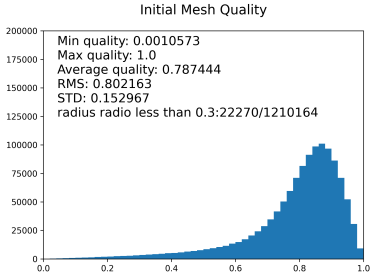
(b) Init min dihedral angle



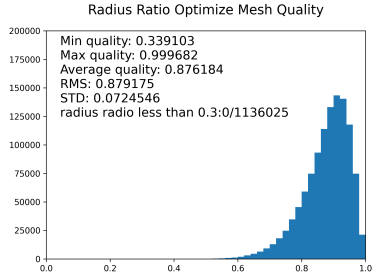
(c) RRE min dihedral angle



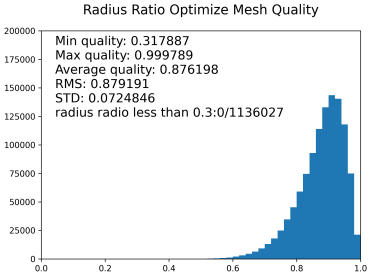
(d) Precondition RRE min dihedral angle



(e) Init quality

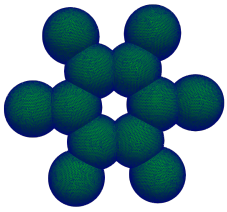


(f) RRE

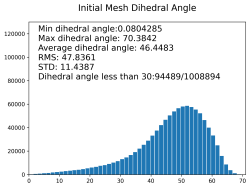


(g) Precondition RRE

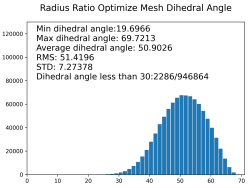
Figure 8: L-shape large scale mesh



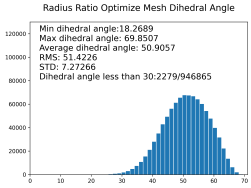
(a) Model



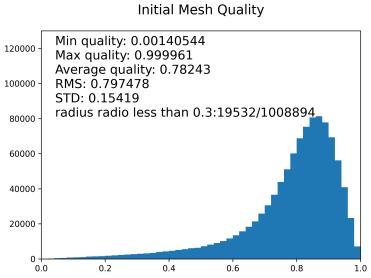
(b) Init min dihedral angle



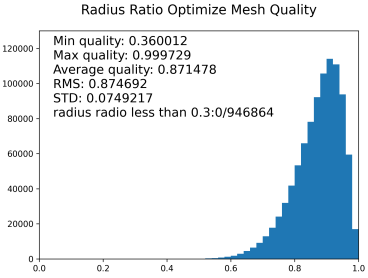
(c) RRE min dihedral angle



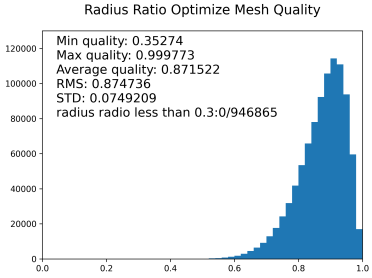
(d) Precondition RRE min dihedral angle



(e) Init quality



(f) RRE



(g) Precondition RRE

Figure 9: Intersection of 12 spheres

Table 3: Comparison of RRE and precondition RRE

Model	Method	Iteration count/ Flip count	Num of cell	min dihedral angle (deg.)	Min radius ratio	Time(sec.)
Sphere	Init	/	677858	0.104	0.002	/
	RRE	385/3	635931	18.70	0.366	1006.18
	Precondition RRE	137/3	635932	18.27	0.367	453.80
Lshape	Init	/	1210164	0.055	0.001	/
	RRE	407/4	1136025	16.59	0.339	1987.53
	Precondition RRE	204/4	1136027	15.36	0.318	1291.91
Intersection of 12 spheres	Init	/	1008894	0.804	0.001	/
	RRE	424/5	946864	19.70	0.360	1721.65
	Precondition RRE	206/5	946865	18.27	0.353	1165.99

Fig. 7, 8, 9 show the results of RRE and preconditioned RRE on larger mesh, with up to millions of elements, for the three test cases. Table 3 reports both the quality and the efficiency. From the figures, the two methods produce very similar distributions of the radius ratio and the dihedral angles. Although the minimum radius ratio and the minimum dihedral angle exhibit slight differences, the overall quality remains comparable. These discrepancies are mainly attributed to the different optimization trajectories induced by the preconditioner, rather than any change in the objective function. This indicates that the preconditioner does not change the final solution of the optimization problem, and the resulting mesh quality is essentially preserved.

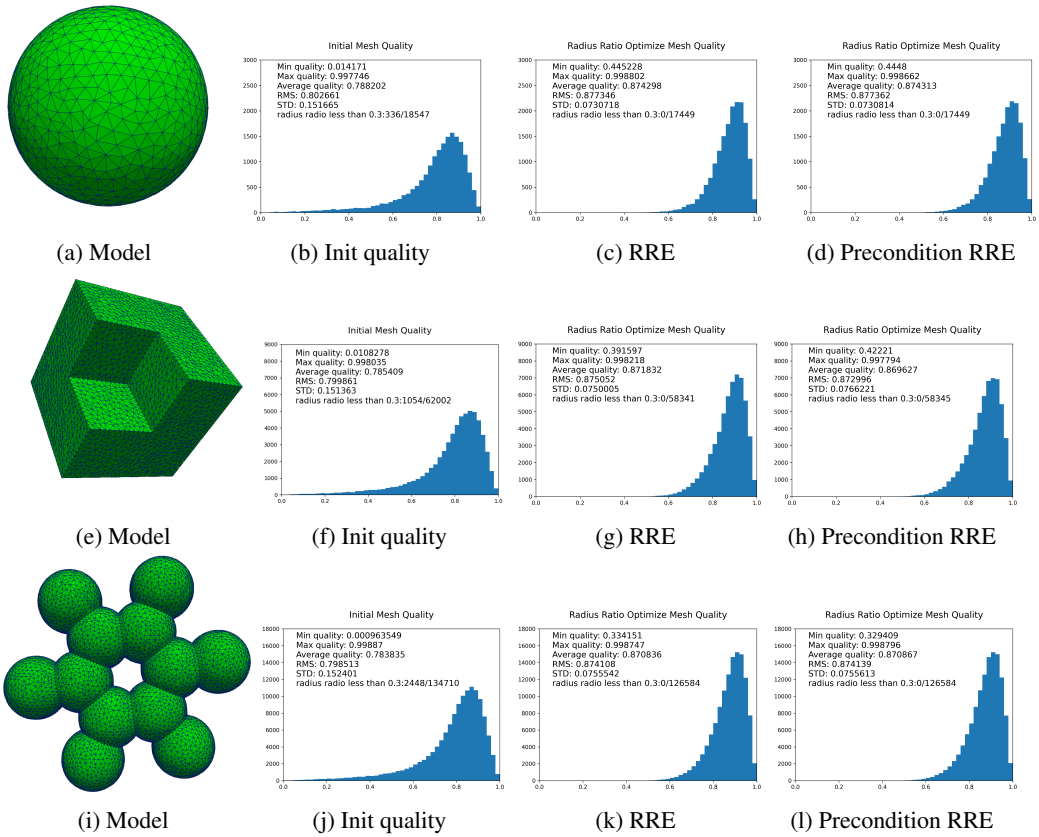
From Table 3, the preconditioner clearly reduces the iteration count and the running time. Compared with small cases, the speedup is more obvious for large problems. This is because, for large mesh, the cost of energy and gradient evaluation dominates. Reducing the number of iterations then leads directly to a clear time saving. In summary, the preconditioner keeps the same optimization result while improving efficiency for large-scale problems.

Table 4: Use PNLCG algorithm instead of PLBFGS algorithm

Model	Method	Iteration count/ Filp count	Num of cell	Min dihedral angle(deg.)	Min radius ratio	Time(sec.)
Sphere	Init	/	18574	0.708	0.014	/
	RRE	113/2	17449	21.88	0.445	8.53
	Precondition RRE	59/2	17449	21.88	0.445	4.77
Lshape	Init	/	62002	0.516	0.011	/
	RRE	381/3	58341	18.67	0.392	83.09
	Precondition RRE	97/3	58345	19.24	0.422	25.29
Intersection of 12 spheres	Init	/	134710	0.230	9.63e-4	/
	RRE	363/3	126584	17.65	0.334	171.34
	Precondition RRE	124/3	126584	17.82	0.329	79.08

The proposed preconditioner is designed to accelerate first-order optimization methods. In the previous examples, we used the PLBFGS method. However, the construction of the preconditioner depends on the structure of the radius ratio energy, not on a specific optimization method. In principle, it can be used with other methods that have a similar iteration structure. To verify this, Fig. 10 and Table 4 show results when the optimizer is replaced by the PNLCG method, for the sphere, L-shaped domain, and intersection of 12 spheres cases. The results show that RRE still improves mesh quality under PNLCG. With the preconditioner, both the iteration count and the running time are reduced, while the resulting mesh quality remains comparable to that obtained without preconditioning. This shows that the preconditioner also works well in the PNLCG framework. It improves the search direction and speeds up convergence. Therefore, the proposed preconditioner is general and can be used with different first-order methods.

Since this work focuses on mesh optimization rather than mesh generation, it is reasonable to assume that the boundary node distribution is well-shaped and the boundary mesh quality is satisfactory. Under this assumption, we fix the boundary nodes and perform optimization only on the interior nodes. Fig. 11 and Table 5 present the corresponding numerical results. The results show that, even with fixed boundary nodes, RRE can still significantly improve the overall mesh quality and effectively enhance low-quality elements. Compared with the case where boundary nodes can move, the improvement is slightly smaller, but still stable and effective. Moreover, since fixing boundary nodes



(a) Model (b) Init quality (c) RRE (d) Precondition RRE

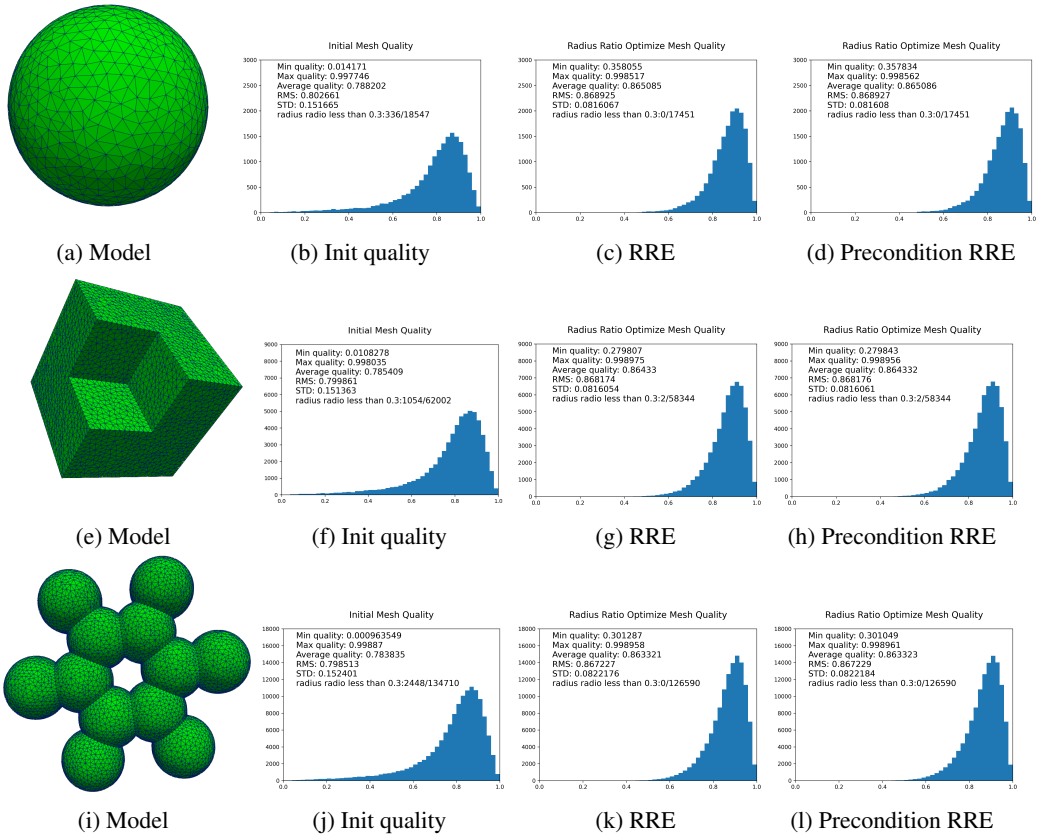
(e) Model (f) Init quality (g) RRE (h) Precondition RRE

(i) Model (j) Init quality (k) RRE (l) Precondition RRE

Figure 10: Use PNLCG algorithm instead of PLBFGS algorithm

Table 5: Fixed boundary point RRE mesh optimization

Model	Method	Iteration count/ Filp count	Num of cell	Min dihedral angle(deg.)	Min radius ratio	Time(sec.)
Sphere	Init	/	18574	0.708	0.014	/
	RRE	95/2	17451	17.18	0.358	5.60
	Precondition RRE	46/2	17451	17.18	0.358	3.34
Lshape	Init	/	62002	0.516	0.011	/
	RRE	154/3	58344	16.68	0.280	34.38
	Precondition RRE	73/3	58344	16.68	0.280	20.51
Intersection of 12 spheres	Init	/	134710	0.230	9.63e-4	/
	RRE	152/5	126590	14.84	0.301	77.95
	Precondiiton RRE	103/5	126590	14.83	0.301	65.59



(a) Model (b) Init quality (c) RRE (d) Precondition RRE

(e) Model (f) Init quality (g) RRE (h) Precondition RRE

(i) Model (j) Init quality (k) RRE (l) Precondition RRE

Figure 11: Fixed boundary point RRE mesh optimization

eliminates the need for boundary movement and projection operations, and reduces the number of degrees of freedom involved in the optimization, the convergence speed is improved and the computational efficiency is higher. These results indicate that, in practical applications where the boundary mesh quality is already satisfactory, adopting a fixed-boundary optimization strategy can further improve computational efficiency while maintaining good optimization performance.

5.3 Anisotropic mesh

For anisotropic mesh, we first generate an initial isotropic mesh and then optimize it according to a given anisotropic metric. Below we present several two-dimensional and three-dimensional examples.

Fig. 12 shows the unit disk with the anisotropic metric $\boldsymbol{M}(\boldsymbol{x}) = \boldsymbol{Q}(\boldsymbol{x})^T \Lambda \boldsymbol{Q}(\boldsymbol{x})$ where

$$\Lambda = \mathrm{diag}(25, 1), \boldsymbol{Q}(\boldsymbol{x}) = \begin{bmatrix} \cos(\phi(\boldsymbol{x})) & -\sin(\phi(\boldsymbol{x})) \\ \sin(\phi(\boldsymbol{x}) & \cos(\phi(\boldsymbol{x}))) \end{bmatrix}$$

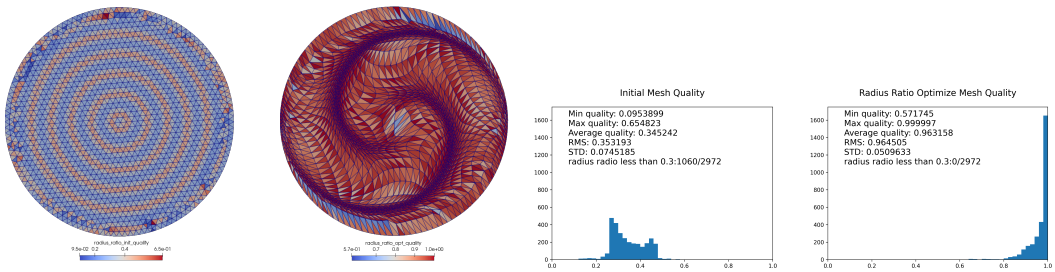
Let $r = \sqrt{x^2 + y^2}, \phi(\boldsymbol{x}) = kr, k = 6$. Under this metric, the mesh forms a spiral anisotropic pattern.

If we modify the metric by setting $\theta = \arctan 2(y, x), \phi(\boldsymbol{x}) = k\theta, k = 6$, the mesh forms a radial anisotropic pattern from the center, as shown in Fig. 13.

Fig. 14 shows a square domain $[0, 1] \times [0, 1]$ with the metric $\boldsymbol{M}(\boldsymbol{x}) = \boldsymbol{Q}(\boldsymbol{x})^T \Lambda \boldsymbol{Q}(\boldsymbol{x})$,where

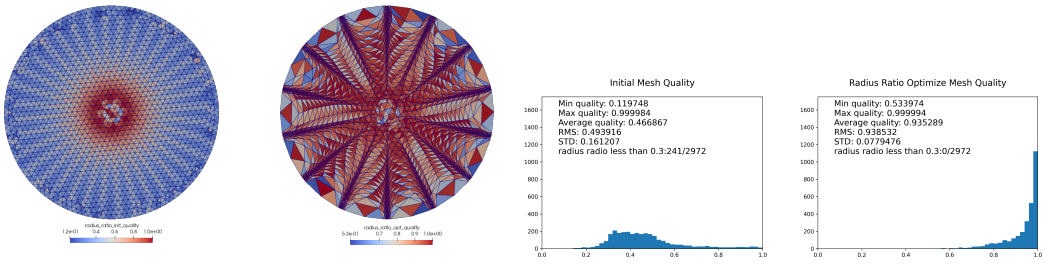
$$\Lambda = \mathrm{diag}(1, 1 + (t-1)\exp(-\frac{f(x,y)^2}{\sigma^2}), f(x, y) = y - 0.5 - 0.15\sin(2\pi x)$$

with parameters $t = 9, \sigma = 0.12$. The first row of $\boldsymbol{Q}(\boldsymbol{x})$ is the unit tangent vector of $f(x, y)$, and the second row is the unit normal vector. This metric stretches the mesh along the curve $\Gamma : y = 0.5 + 0.15\sin(2\pi x)$ and produces a smooth band structure.



(a) Init mesh (b) Optimized mesh (c) Init quality (d) RRE quality

Figure 12: Spiral anisotropic mesh



(a) Init mesh (b) Optimized mesh (c) Init quality (d) RRE quality

Figure 13: Radial anisotropic mesh

Fig. 15 shows the unit sphere with the metric $\boldsymbol{M}(\boldsymbol{x}) = \lambda_r \boldsymbol{r}\boldsymbol{r}^T + \lambda_t(\boldsymbol{I} - \boldsymbol{r}\boldsymbol{r}^T)$, where

$$\boldsymbol{r}(\boldsymbol{x}) = \frac{\boldsymbol{x}}{\|\boldsymbol{x}\| + \varepsilon}, \lambda_r = 1, \lambda_t = 16$$

This metric stretches the mesh in the radial direction.

Fig. 16 shows another metric $\boldsymbol{M}(\boldsymbol{x}) = \lambda_n(d)\boldsymbol{r}\boldsymbol{r}^T + \lambda_t(\boldsymbol{I} - \boldsymbol{r}\boldsymbol{r}^T)$ on the unit sphere where

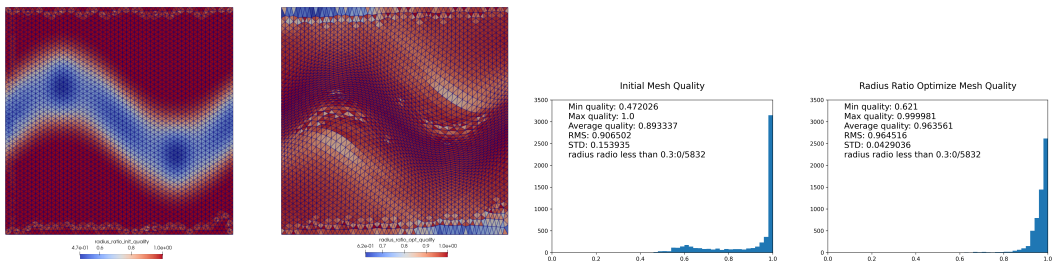
$$d(\boldsymbol{x}) = 1 - \|\boldsymbol{x}\|, \boldsymbol{r}(\boldsymbol{x}) = \frac{\boldsymbol{x}}{\|\boldsymbol{x}\| + \varepsilon}, \lambda_n(d) = 1 + 20e^{-10d}, \lambda_t = 1$$

This metric produces a boundary layer structure with finite thickness.

Fig. 17 shows the cube domain $[0, 1]^3$ with the metric $\boldsymbol{M} = \text{diag}(m_0, m_1(\boldsymbol{x}), m_2(\boldsymbol{x}))$ where

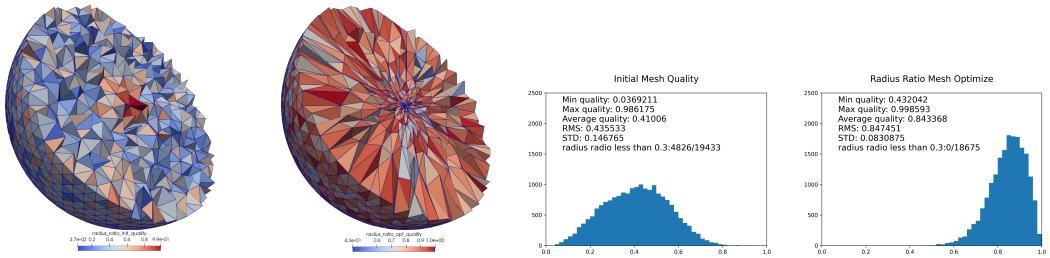
$$m_0 = 3, m_1(\boldsymbol{x}) = 1 + (t-1)\exp(-\frac{(y-0.5)^2}{2\sigma^2}), m_2(\boldsymbol{x}) = 1 + (t-1)\exp(-\frac{(z-0.5)^2}{2\sigma^2})$$

with $\sigma = 0.05, t = 10$. This metric introduces anisotropic regions near the planes $y = 0.5$ and $z = 0.5$, forming two intersecting anisotropic bands.



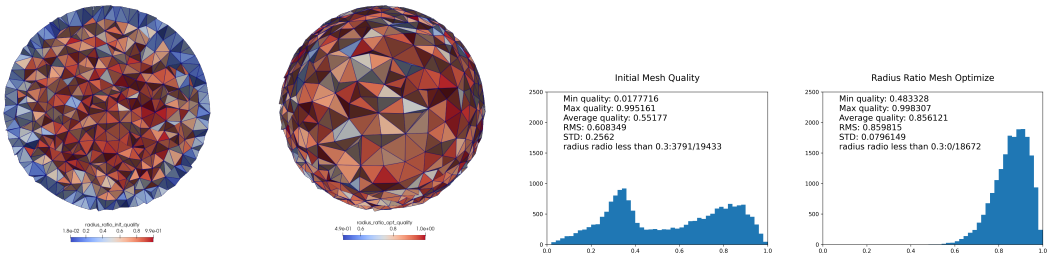
(a) Init mesh (b) Optimized mesh (c) Init quality (d) RRE quality

Figure 14: Curve-induced anisotropic mesh



(a) Init mesh (b) Optimized mesh (c) Init quality (d) RRE quality

Figure 15: Unit sphere radial anisotropic mesh

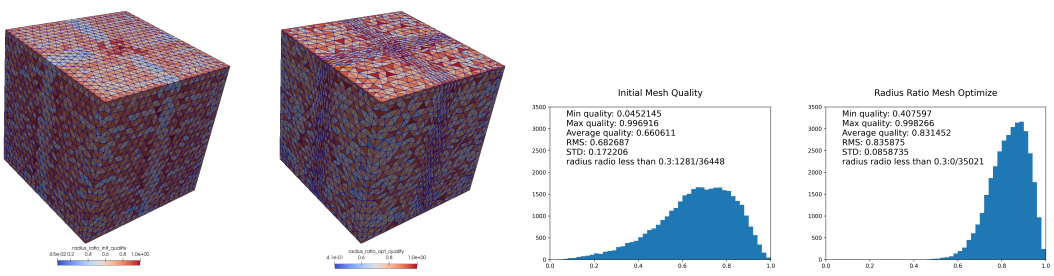


(a) Init mesh (b) Optimized mesh (c) Init quality (d) RRE quality

Figure 16: Unit sphere boundary layer anisotropic mesh

These examples show that the radius ratio based optimization method adapts well to anisotropic cases. For different metric tensors, the method captures both direction and scale changes, and aligns the mesh elements with the main anisotropic directions. In terms of element shape, the optimized tetrahedra tend to ideal shapes in the metric space. In strongly anisotropic regions, elements are stretched along the main directions, while in weak anisotropic regions, they return to near isotropic shapes. In all examples, the mesh quality is clearly improved. The minimum and average radius ratios increase, and low-quality elements are greatly reduced. This shows that the method has good shape optimization capabilities while maintaining anisotropic features.

Finally, Table 6 reports the number of cell, iteration counts, and running times for the two-dimensional and three-dimensional anisotropic cases. In general, the computation time increases with mesh size. The number of iterations depends on the metric. For strongly anisotropic cases (such as the radial metric on the unit sphere), the iteration count is higher. Even so, the method converges in a reasonable number of iterations in all cases. Overall, the proposed method shows good efficiency and stability for different scales and types of anisotropic problems.



(a) Init mesh (b) Optimized mesh (c) Init quality (d) RRE quality

Figure 17: Cube anisotropic mesh

Table 6: Anisotropic example optimization results

Model	Num of cell	Iteration count	Time(sec.)
Unit disk: Spiral anisotropic mesh	2972	203	0.70
Unit disk: Radial anisotropic mesh	2972	182	0.65
square: Curve-induced anisotropic mesh	5832	148	1.10
Unit sphere: radial anisotropic mesh	18675	471	78.26
Unit sphere: boundary layer anisotropic mesh	18672	253	42.29
Cube: anisotropic mesh	35021	149	40.36

6 Conclusion and further work

This paper proposes a simplex mesh optimization method based on the radius ratio energy. The method can effectively suppress slivers and improve the overall mesh quality. Based on the structure of the gradient of the radius ratio energy, we also construct a preconditioner. The preconditioned optimization reduces the number of iterations and speeds up convergence.We further extend the radius ratio energy to the anisotropic case and define an energy function suitable for anisotropic mesh. As a result, the RRE method can be applied to both isotropic and anisotropic mesh optimization.In future work, we plan to extend the proposed method to high-order mesh and further improve computational efficiency by leveraging GPU-based parallel computing.

Declaration of competing interest

The authors declare that they have no known competing financial interests or personal relationships that could have appeared to influence the work reported in this paper.

Acknowledgement

This work was supported in part by the National Key R&D Program of China (2024YFA1012600), the National Natural Science Foundation of China (NSFC) (Grant No. 12371410, 12261131501), and the Graduate innovation Project of Xiangtan University(Grant No.XDCX2024Y183)

References

[1] M. Bern and D. Eppstein. Mesh generation and optimal triangulation. In *Computing in Euclidean geometry*, pages 47–123. World Scientific, 1995.

[2] J. C. Caendish, D. A. Field, and W. H. Frey. An apporach to automatic three-dimensional finite element mesh generation. *International journal for numerical methods in engineering*, 21(2):329–347, 1985.

[3] L. Chen. Mesh smoothing schemes based on optimal delaunay triangulations. In *IMR*, pages 109–120. Citeseer, 2004.

[4] L. Chen and M. Holst. Efficient mesh optimization schemes based on optimal delaunay triangulations. *Computer Methods in Applied Mechanics and Engineering*, 200(9-12):967–984, 2011.

[5] L. Chen and J.-c. Xu. Optimal delaunay triangulations. *Journal of Computational Mathematics*, pages 299–308, 2004.

[6] S.-W. Cheng, T. K. Dey, H. Edelsbrunner, M. A. Facello, and S.-H. Teng. Sliver exudation. *Journal of the ACM (JACM)*, 47(5):883–904, 2000.

[7] S.-W. Cheng, T. K. Dey, J. Shewchuk, and S. Sahni. *Delaunay mesh generation*. CRC Press Boca Raton, 2013.

[8] L. P. Chew. Guaranteed-quality delaunay meshing in 3d (short version). In *Proceedings of the thirteenth annual symposium on Computational geometry*, pages 391–393, 1997.

[9] Y.-H. Dai and Y. Yuan. A nonlinear conjugate gradient method with a strong global convergence property. *SIAM Journal on optimization*, 10(1):177–182, 1999.

[10] Q. Du, V. Faber, and M. Gunzburger. Centroidal voronoi tessellations: Applications and algorithms. *SIAM review*, 41(4):637–676, 1999.

[11] R. Eymard, T. Gallouët, and R. Herbin. Finite volume methods. *Handbook of numerical analysis*, 7:713–1018, 2000.

[12] A. Fabri, G.-J. Giezeman, L. Kettner, S. Schirra, and S. Schönherr. On the design of cgal a computational geometry algorithms library. *Software: Practice and Experience*, 30(11):1167–1202, 2000.

[13] R. Fletcher and C. M. Reeves. Function minimization by conjugate gradients. *The computer journal*, 7(2):149–154, 1964.

[14] C. Geuzaine and J.-F. Remacle. Gmsh: A 3-d finite element mesh generator with built-in pre-and post-processing facilities. *International journal for numerical methods in engineering*, 79(11):1309–1331, 2009.

[15] W. W. Hager and H. Zhang. A survey of nonlinear conjugate gradient methods. *Pacific journal of Optimization*, 2(1):35–58, 2006.

[16] J. C. Hateley, H. Wei, and L. Chen. Fast methods for computing centroidal voronoi tessellations. *Journal of Scientific Computing*, 63(1):185–212, 2015.

[17] M. R. Hestenes, E. Stiefel, et al. Methods of conjugate gradients for solving linear systems. *Journal of research of the National Bureau of Standards*, 49(6):409–436, 1952.

[18] B. M. Klingner and J. R. Shewchuk. Aggressive tetrahedral mesh improvement. In *Proceedings of the 16th international meshing roundtable*, pages 3–23. Springer, 2007.

[19] P. Knupp. Introducing the target-matrix paradigm for mesh optimization via node-movement. *Engineering with Computers*, 28(4):419–429, 2012.

[20] P. Knupp. Metric type in the target-matrix mesh optimization paradigm. Technical report, Lawrence Livermore National Lab.(LLNL), Livermore, CA (United States), 2020.

[21] X. Li. *Sliver-free three dimensional delaunay mesh generation*. University of Illinois at Urbana-Champaign, 2001.

[22] D. C. Liu and J. Nocedal. On the limited memory bfgs method for large scale optimization. *Mathematical programming*, 45(1):503–528, 1989.

[23] O. E. Livne and A. Brandt. Lean algebraic multigrid (lamg): Fast graph laplacian linear solver. *SIAM Journal on Scientific Computing*, 34(4):B499–B522, 2012.

[24] D. S. Lo. *Finite element mesh generation*. CRC press, 2014.

[25] S. Lo. Optimization of tetrahedral meshes based on element shape measures. *Computers & structures*, 63(5):951–961, 1997.

[26] R. Löhner and P. Parikh. Generation of three-dimensional unstructured grids by the advancing-front method. *International Journal for Numerical Methods in Fluids*, 8(10):1135–1149, 1988.

[27] J. L. Nazareth. Conjugate gradient method. *Wiley Interdisciplinary Reviews: Computational Statistics*, 1(3):348–353, 2009.

[28] J. Nocedal and S. J. Wright. *Numerical optimization*. Springer, 1999.

[29] S. J. Owen. A survey of unstructured mesh generation technology. *IMR*, 239(267):15, 1998.

[30] E. Polak and G. Ribiere. Note sur la convergence de méthodes de directions conjuguées. *Revue française d'informatique et de recherche opérationnelle. Série rouge*, 3(16):35–43, 1969.

[31] J. W. Ruge and K. Stüben. Algebraic multigrid. In *Multigrid methods*, pages 73–130. SIAM, 1987.

[32] M. S. Shephard and M. K. Georges. Automatic three-dimensional mesh generation by the finite octree technique. *International Journal for Numerical methods in engineering*, 32(4):709–749, 1991.

[33] J. R. Shewchuk. Two discrete optimization algorithms for the topological improvement of tetrahedral meshes. *Unpublished manuscript*, 65:2–7, 2002.

[34] J. R. Shewchuk. Unstructured mesh generation. *Combinatorial Scientific Computing*, 12(257):2, 2012.

[35] H. Wei and Y. Huang. Fealpy: Finite element analysis library in python. https://github.com/weihuayi/ fealpy, Xiangtan University, 2017-2023.

[36] M. Yerry and M. Shephard. A modified quadtree approach to finite element mesh generation. *IEEE Computer Graphics and Applications*, 3(01):39–46, 1983.